The Astrophysical Journal Supplement Series, 200:21 (21pp), 2012 June doi:10.1088/0067-0049/200/2/21

THE GALACTIC PLANE INFRARED POLARIZATION SURVEY (GPIPS): DATA RELEASE 1

Dan P. Clemens, M. D. Pavel, and L. R. Cashman
Institute for Astrophysical Research, Boston University, 725 Commonwealth Ave, Boston, MA 02215, USA;
clemens@bu.edu, pavelmi@bu.edu, lcashman@bu.edu
Received 2012 March 15; accepted 2012 April 19; published 2012 May 31

ABSTRACT

The Galactic Plane Infrared Polarization Survey (GPIPS) covers 76 deg^2 of the first Galactic quadrant midplane, $18^\circ \leqslant \ell \leqslant 56^\circ$ and $-1^\circ \leqslant b \leqslant +1^\circ$, in *H*-band (1.6 μm) linear polarimetry to reveal the plane-of-the-sky orientation of the magnetic field in diffuse and denser atomic and molecular clouds. The Survey consists of 3237 overlapping 10×10 arcmin fields observed using the Mimir instrument on the 1.8 m Perkins telescope. Here, the first community release of GPIPS data for 559 fields (17% of the Survey) is announced and basic characteristics are described. Data products consist of *H*-band stellar photometry and polarimetry as well as combined images. The formats and contents of the products are described and quality cuts are explored to provide insight into opportunities and limitations of the data. The Survey probes to distances as far as the Galactic bulge, revealing magnetic field properties that correlate with spiral arms and also show significant small-scale structure. The polarizations are classified into three "usage" samples, based on stellar brightness and polarimetric uncertainty. The brightest, lowest uncertainty polarizations are suitable for individual use and direct magnetic field mapping. The next two fainter samples are useful, once averaged, for probing magnetic fields to greater distances, albeit with lower resolution. Based on this release, the full GPIPS data set will number about 5.6 million stars, with more than 1 million in the high-quality sample. This increases, by many orders of magnitude, the number of polarimetric probes of the Milky Way's magnetic field.

Key words: Galaxy: disk – ISM: magnetic fields – magnetic fields – polarization – surveys – techniques: polarimetric

Online-only material: color figures

1. INTRODUCTION

The magnetic field in the quiescent and star-forming regions and cool interstellar medium (ISM) of the Galactic disk has been difficult to probe to date due to the presence of optically opaque dust clouds and the absence of any uniform magnetic field survey at arcmin to arcsec angular resolution. The Galactic Plane Infrared Polarization Survey (GPIPS) was designed to resolve these issues by revealing the magnetic field in the disk with finer detail and to greater distances than ever before. The Survey does so using near-infrared (NIR) *H*-band polarimetry of background starlight to reveal the plane-of-the-sky projected magnetic field orientations across a 76 deg^2 zone encompassing the midplane of most of the first Galactic quadrant.

Companion papers describe the science-driven design of GPIPS and data collection methods (Clemens et al. 2012b, hereafter Paper I) and the extensive calibration observations and analyses in support of GPIPS (Clemens et al. 2012a, hereafter Paper II) that yield high-quality, high-reliability linear polarimetry for the stars in the Survey fields.

GPIPS also has a top-level goal of rapidly delivering science-quality data products to the astronomical community to support a multitude of analyses. In this paper, an initial, representative set of observing runs were selected for data products release and the forms and contents of these data products are described. In addition to providing the community access to these unique data, this first data release (hereafter DR1) of data products defines the templates for all future GPIPS data releases (which will be electronic, only).

The following sections describe the selection of the observing runs comprising DR1, some of the basic characteristics of the data drawn from these runs, and the application of criteria that ensure high data quality. Next, example science contained in the (10×10 arcmin) field-based and stellar-based aspects of DR1 are explored, including large-scale and medium-scale Galactic magnetic field behavior. The polarimetric data are subdivided into "usage" samples, to identify stars that individually may be used to reveal magnetic field directions as well as those that require being included in averages of many stars in order to reveal magnetic field properties. Concerns and caveats for potential users of GPIPS data are identified, prior to the paper summary. The forms and example contents of the GPIPS DR1 data products are presented in the Appendix.

2. SELECTION OF DR1 FIELDS

GPIPS observations began in 2006 and continue as of this writing. They consist of several multi-night observing runs conducted each year primarily during May–June and September–October using the Mimir instrument (Clemens et al. 2007) on the 1.8 m Perkins telescope, located outside Flagstaff, AZ. While the basic observing and calibration methods and approaches have not changed greatly over the course of the Survey, incremental improvements in the detector, instrument, and telescope systems have led to better data consistency. Hence, in selecting a subset of the observations for DR1, recent observing runs were favored. However, the data processing pipelines (Paper I) require significant run times, making the most recently obtained data not yet available for the analyses described below. As a compromise, GPIPS data from the four observing runs between 2010 May and 2011 May were selected for DR1. The properties of these observing runs are summarized in Table 1. A total of 779 of the 3237 fields comprising GPIPS were observed over the 49 nights spanned in these four observing runs.

2.1. Culling of Candidate Fields

Observations were only conducted on clear nights (i.e., no cirrus clouds), but other problems such as poor seeing and wind

Table 1
GPIPS Observing Runs in DR1

Run Designation (YYYYMM) (1)	UT Dates (MMDD–MMDD) (2)	Observed GPIPS Fields (3)	DR1 Surviving GPIPS Fields (4)
201005	0522–0605	217	153
201006	0618–0630	278	188
201009	0918–0930	238	193
201105	0514–0521	46	25
Totals	49	779	559
Ave per night		15.9	11.4

shake of the telescope that affect the observations did occur. As noted in Paper I, GPIPS observations are electronically scripted, with minimal operator intervention. As each of the 96 (nominal, though observations in the early years included up to 117) images comprising one observation of a 10 × 10 arcmin field arrive with a 5–7 s cadence, real-time image evaluation was not performed. Instead, the data processing pipeline (Paper I) conducted numerous data quality tests on the individual images and on the collection of images making up each field's polarimetric observation. This leads to several levels of data culling and field rejection in order to ensure high quality of the Survey data.

Images with stellar point-source functions (PSFs) showing Gaussian-fitted major/minor axis width ratios in excess of 1.5 were rejected. This removed almost all examples of wind shake and telescope tracking problems. Each field was observed at six (seven in the early years) sky-dither positions with 16 (17 in the early years by taking two HWP 0°) images representing four independent polarization position angles (IPPAs), each through a different position angle of Mimir's *H*-band half-wave-plate (HWP). This represents a fourfold HWP angle redundancy, in addition to the sixfold sky dither redundancy. If, after astrometric registration and computation of the average images for each HWP position angle, fewer than the minimum four IPPAs survived (Paper I), that field was judged a failed observation. Hence, at this first level of culling, of the 779 GPIPS fields observed, 766 fields completed the software pipeline data processing steps described in Paper I.

Additional checks tested for pointing errors, incursions into the imaging field by the autoguider pickoff mirror probe, and duplicate field observations. All of these, except the latter, led to removal of the offending fields and returning them to the observing queue.

An additional quality cut was applied to insure uniform, high-quality DR1 data. It counted the number of images making up a field observation that were flagged by the pipeline processing software as unusable. If that number exceeded 5 (of the 96–117 images), then the observation of that field was judged to have failed.

2.2. Seeing Criterion

The final quality cut was based on the average seeing measured for each field. After the 16 HWP angle based sky-averaged images were calculated, and these were themselves averaged to form the final combined photometric image for the field, stars within the combined image were fit with two-dimensional Gaussians to evaluate the PSF widths. These were further corrected for the broadening effects of the 0.58 arcsec Mimir detector array pixels to yield corrected widths. The distribution of the harmonic means of the corrected widths for the major and minor axes for the 766 fields is shown in Figure 1, as is its cumulative distribution function. The median width is 1.5 arcsec and some 16% of the sample shows widths in excess of 2.0 arcsec. A plot of the number of stars detected in each field (not shown), for either photometry or polarimetry, shows a marked decrease for PSF widths larger than 2 arcsec, but is mostly flat with stellar profile width below that value. Hence, to achieve uniform data quality, fields showing stellar PSFs with widths greater than 2 arcsec were culled and returned to the observing queue.

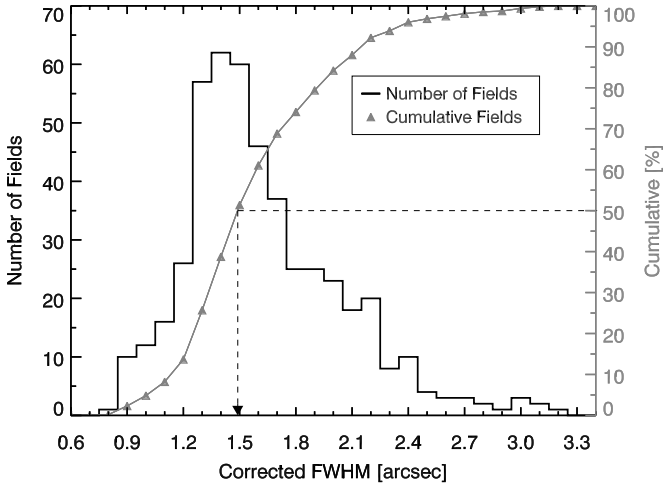

Figure 1. Seeing distribution (black) and cumulative seeing (gray) for the candidate fields. Horizontal axis displays the average stellar profile FWHM, corrected for the detector pixel sampling. The median seeing is just under 1.5 arcsec.

A weaker correlation remains between the PSF widths and Galactic longitude. This is a signature of the observing strategy, one that favored observing fields at lower Galactic longitudes closer to their transits (minimum air mass for these low elevation fields) while observing higher longitudes as they rose or set ($\leqslant$2 air masses) to best utilize each sidereal pass of the GPIPS sky region. Given the higher stellar densities in the lower longitude fields, this small air mass bias helps preserve the numbers of stars with measured polarizations at the lower longitudes. Re-observation of the higher longitude fields that show stellar widths greater than 2 arcsec should help soften this effect in the full GPIPS data set.

3. OBSERVED PROPERTIES OF THE DR1 FIELDS

After removing all the fields showing any of the problems described above, a total of 559 GPIPS fields survived to become the DR1 set. The distribution of these fields in Galactic coordinates, overlaid on the full distribution of 3237 GPIPS field centers, is shown in Figure 2. The distribution reveals that the DR1 field centers were observed neither uniformly nor consecutively, but instead reflect scientific priorities. In the early Survey years, fields containing known stellar clusters, pulsars, and the $b = 0°$ midplane were observed first. Hence, in DR1, mostly contiguous off-plane zones were surveyed to connect previously observed sky fields. While representing an obviously biased sample drawn from the full GPIPS set (e.g., $b = 0°$ is greatly underrepresented), there are a number of important and interesting aspects revealed in the DR1 fields.

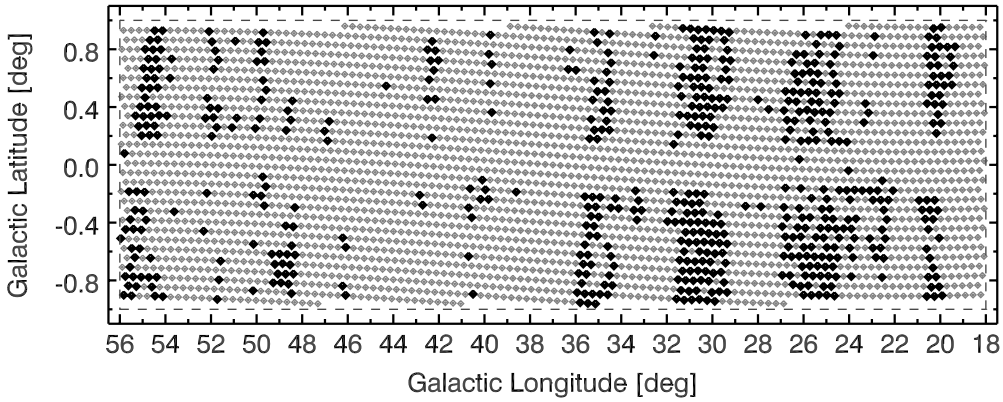

Figure 2. Distribution of field centers in Galactic coordinates, with the GPIPS field centers in gray and DR1 field centers in black. Note the artificial elongation of the b axis relative to the ℓ axis.

3.1. Plate Scale, Sky Brightness, Sky Noise, and Field Polarization

The pipeline data processing (Paper I) performed astrometry for each image, using the Two Micron All Sky Survey (2MASS) point sources (Skrutskie et al. 2006) in each Mimir field as the reference frame. The distribution of the derived plate scales for the DR1 fields shows a full-width at half-maximum (FWHM) width of 0.12% about a mean of 0.5788 arcsec per pixel, representing no worse than 0.5 pixel uncertainty between neighboring images out to the corners of the field of view (FOV).

The near-infrared (NIR) *H*-band contains strong telluric OH emission lines that vary in brightness and the atmosphere also shows transmission variations that contribute sky noise to the GPIPS observations. The pipeline processing extracted stellar brightnesses *above* the local sky background, so the stellar photometry and polarimetry ought to be independent of OH airglow. Characterization and removal of the other aspect, sky noise, is important however, and represents a core component of the pipeline data processing (Paper I). The range of sky brightness in the DR1 set spans a factor of five, with a median value of about 450 photoelectrons per pixel per second. This contributes some Poisson noise to the stellar photometry, but at levels smaller than those generated by most of the stars themselves. We find no correlation between sky brightness and the time-resolved component of sky noise that was produced by sky transmission variations.

The sky noise histogram and its cumulative distribution function are shown in Figure 3. The median sky noise measured was just over 0.6% and rarely exceeded 1%. However, not removing this resolved noise would have limited the polarimetric precision and raised the polarization noise floor achievable with GPIPS. So, once identified, this resolved sky noise was removed from the images by suitable rescaling, as described in Paper I. There is no correlation between the stellar PSF widths and sky noise for widths under two arcsec.

Field polarization (FP) is the term introduced in Paper I to describe the mean polarization seen for the ensemble of stars in a single 10×10 arcmin field. It is measured during the image-to-image stellar brightness matching process that also determined the sky noise discussed above. Because FP has a distinct and repetitive signature with HWP angle, it could be isolated from the non-repetitive sky noise. It was crucial to identify and remove the FP before determining the sky noise correction, so that large-scale polarization values were not lost in the pipeline processing (see discussion in Paper I). High FP values generally correlate with well-aligned polarization vectors across a field, while low FP values can signify weak polarizations, sparse stellar densities, or highly dispersed polarization position angles.

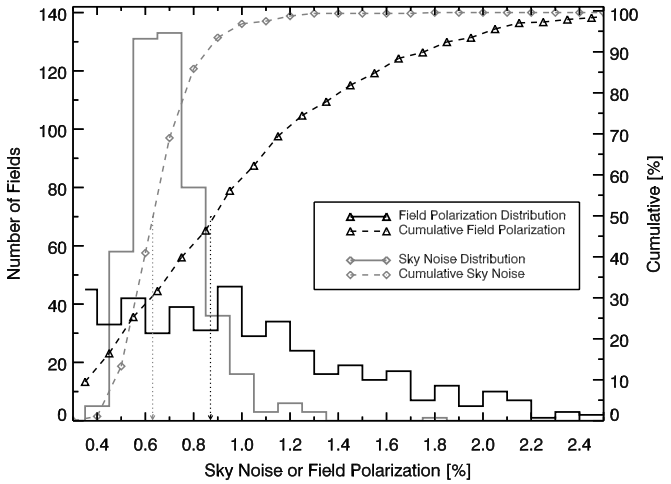

Figure 3. Sky noise and field polarization histograms and cumulative probability distributions. Sky noise curves are shown in gray; field polarization curves are in black.

The histogram of DR1 FP values and the cumulative FP distribution are also shown in Figure 3. The FP distribution is very different in nature from the sky noise distribution, though the FP median of 0.8% is not much larger than the sky noise median. The fitting that revealed each field's polarization also permitted uncertainty determinations, and the mean FP uncertainty of about 0.08% shows that the typical FP value is a well-determined quantity. The caveat is that the sky noise and FP uncertainty are correlated, as both are determined from the residuals of the image-to-image brightness variations after the FP and other regular variations were removed.

3.2. Field-to-field Stellar Match Quality

The GPIPS observing strategy collects images for 10×10 arcmin sized fields using a 9×9 arcmin set of field centers (Paper I), providing adequate overlap so as to avoid gaps due to normal telescope pointing errors. The resulting overlap generates a small subsample of stars for which more than one GPIPS observation exist. Such stars could potentially be used to study photometric or polarimetric temporal variability or the observations could be combined to improve signal-to-noise ratio (S/N; photometric and polarimetric).

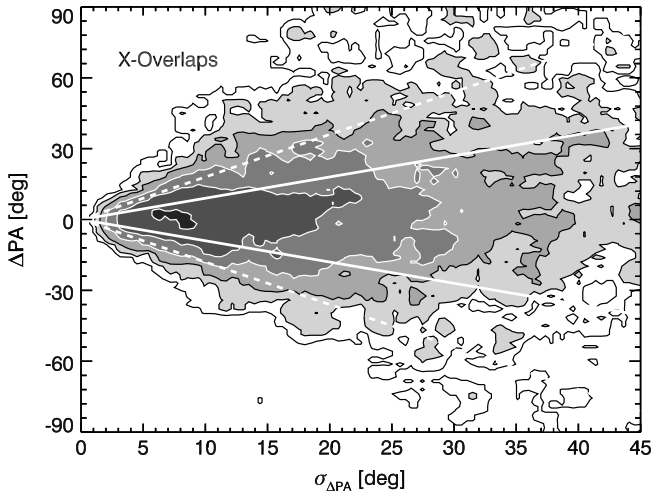

Figure 4. Polarization position angle difference ΔPA vs. its uncertainty $\sigma_{\Delta PA}$, for observations of UF = 1 stars in *X* (R.A.) overlapping images. The vertical axis represents the signed difference in P.A. values for the same star seen at the eastern limit of the field and seen in an overlapping image at the western limit. The horizontal axis represents the propagated uncertainty computed from the individual stellar P.A. uncertainties for each matched stellar pair. The solid white lines have unity slopes and the dashed lines have slopes of two. Contours begin at 90% of the peak stellar density and fall by half for each subsequent contour.

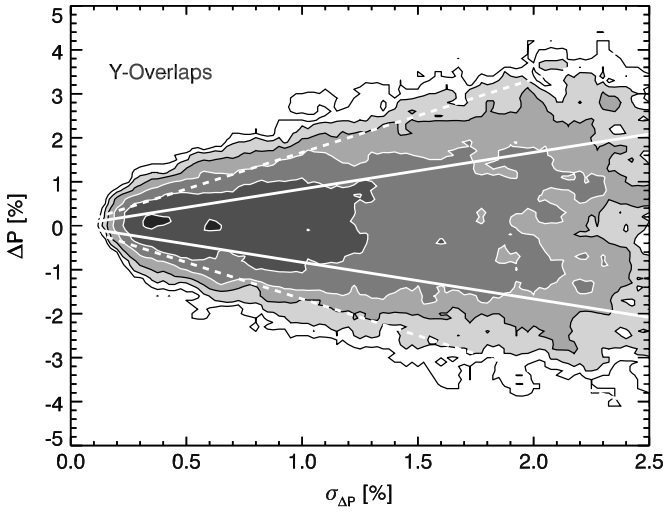

Figure 5. Similar to Figure 4 for *Y* (Decl.) image overlaps and displayed for the difference in measured polarization percentage ΔP vs. the propagated uncertainty of that difference $\sigma_{\Delta P}$.

These overlaps were analyzed to test for potential calibration errors across the FOV resulting from the three-step polarimetric calibration scheme described in Paper II. We sought to test the degree to which the polarimetric properties measured for a star near one edge of the FOV would be measured equally well along a different edge of the FOV—since the edges, and corners, are where the instrumental polarization corrections are greatest and most uncertain (Paper II). Also, some fields were re-observed, offering the opportunity to examine whether the polarimetric variations for stars observed onto nearly identical detector locations behaved as predicted, based on their stellar brightnesses (i.e., whether their difference behavior is consistent with being mostly due to the Poisson noise from the stars and their backgrounds). These tests were performed with the larger, 766-member, pre-DR1 set of fields.

Pairs of these neighboring fields with small (∼30–60 arcsec) overlaps were identified by matching stellar equatorial positions and comparing their tabulated detector positions. Of all the star pairs showing overlaps, those selected for examination in the following tests all had $m_H \leqslant 12.5$ mag and polarimetric uncertainties $\sigma_P \leqslant 2\%$ (i.e., were drawn from the high-quality UF = 1 sample—see Section 4.2.1).

Two stellar subsamples were initially developed: those with detector overlaps at the *X*-axis (R.A.) edges and those with *Y*-axis (decl.) overlaps. Signed differences of key properties were calculated, such that values for stars appearing at the *X*-axis maximum edge were subtracted from the values for stars appearing at the *X*-axis minimum edge, and similarly for the *Y*-axis sample. Uncertainties in the predicted difference properties were also propagated from the input value uncertainties. Subsequently, a third subsample was developed from the fields that had been re-observed, that is, showing nearly no *X*- or *Y*-axis offsets.

Three starlight quantities were examined for each matching star pair: the polarization position angle; the polarization percentage; and the *H*-band photometric magnitude. Each of these was examined in plots of the difference in each quantity for stars matching in *X*, *Y* or in the no-offset fields versus the propagated uncertainties of these quantities.

Figure 4 shows the degree to which, for the *X*-overlap (R.A.) sample, re-observation of the same stars at the left and right sides of the FOV returned polarization position angles that agreed with each other (ΔPA), compared to the propagated uncertainty of those differences ($\sigma_{\Delta PA}$). In the figure, the base two logarithmic contours of stellar density show that most of these stars fall within the region delineated by the two solid white lines. These lines have unity slopes and identify where the difference in the P.A. values for two measurements are equal to the propagated uncertainty for those measurements. The dashed lines have twice the slopes (e.g., $\pm 2\sigma$ lines) and contain almost all of the stellar density in the plot. Similar plots for the *Y*-overlap sample and for the no-offset overlap sample (not shown) are virtually identical.

Similarly, Figure 5 shows, for the *Y* (decl.) overlap sample, the differences in polarization percentage ΔP versus its propagated uncertainty $\sigma_{\Delta P}$. Again, the polarization properties are well explained by the uncertainties, indicating that the chief source of uncertainty is the Poisson-limited nature of the stellar polarization observations. The same quantities plotted for the *X* and no-offset overlap samples (not shown) look virtually identical.

Departures from the excellent behavior of the polarization quantities are seen for the photometric matches, however. Figure 6 shows how repeat observations of the same stars, for essentially no change in pointing, results in quite different *H*-band magnitudes, compared to the propagated (internal) uncertainties for those differences. The same behavior is seen in the *X*- and *Y*-overlap samples (not shown). There appears to be an extra 0.04–0.05 mag of photometric uncertainty, compared to the internal uncertainties propagated. The departures arise from a combination of the higher 2MASS uncertainties for bright stars and the lack of any color corrections or transformations for GPIPS *H*-band magnitudes. We therefore tabulate both the internal (i.e., within a single field) magnitude uncertainties as well as estimates of the external uncertainties, computed as the root square sum of the former with a fixed value of 0.045 mag. This limits the photometric accuracy of GPIPS stellar entries to no better than that value when comparing to other catalogs, but plays no role in the polarimetric precision, as discussed in Paper II.

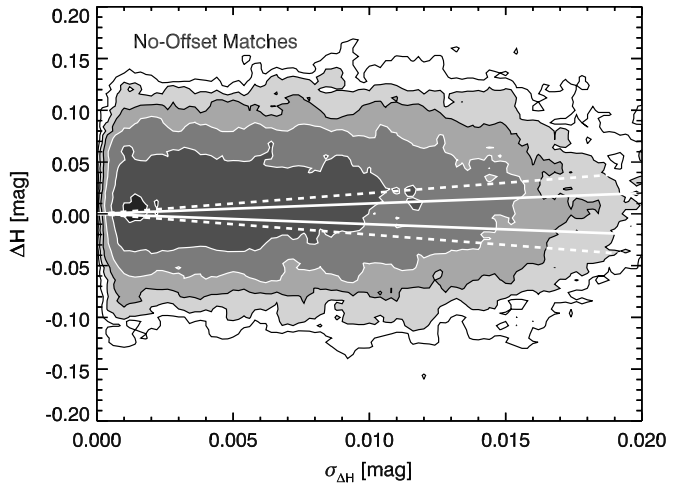

Figure 6. Similar to Figure 4 for the no-offset overlap of the fields that were observed more than once and displaying the difference in the H-band stellar magnitudes ΔH vs. the propagated uncertainty of that difference $\sigma_{\Delta H}$. Agreement with the white lines is improved when a 45 mmag external uncertainty is added in quadrature with the internal photometric uncertainties.

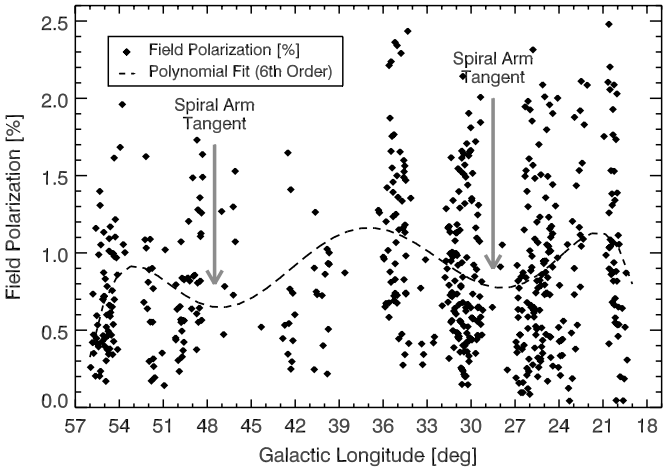

Figure 7. Field polarization FP vs. Galactic longitude ℓ for the DR1 fields. Also shown is a sixth-order polynomial (dashed line) and the approximate longitudes for two spiral arm tangents. The one near $\ell = 50°$ corresponds to the Sagittarius arm. The one near $\ell = 30°$ is either the beginning of the Scutum arm or the end of the long bar from the Galactic Center. FPs appear to decrease in the vicinities of the tangent directions.

3.3. Galactic Magnetic Field at Low Resolution: FP versus Longitude

The FP values can serve as a low-resolution first look at the large-scale polarization properties revealed in the GPIPS fields. When FP was plotted versus Galactic latitude b (not shown), only a very weak trend of smaller FP values at the most extreme limits of b (to $\pm 1°$) was seen. An exponential fit of FP with $|b|$ revealed a scale height of about 2°, but with a very weak correlation probability. For DR1 and when using FP, the magnetic field of the Milky Way disk does not appear to decrease in overall FP (which might be considered a partial proxy for field strength) with latitude to the limits surveyed. This requires a disk magnetic scale height of at least 70 pc, if the mean distance probed is 2 kpc, or 175 pc to 5 kpc.

It is with Galactic longitude ℓ that the FP quantity begins to reveal new magnetic structure in the Milky Way. Figure 7 shows the distribution of FP values versus longitude for the DR1 sample (as filled diamonds). The sparse and uneven longitude sampling is due to the non-uniform coverage of the DR1 sample, described above. An F-test supported sixth-order polynomial fit to the FP data is also shown and reveals two broad longitude zones exhibiting lower FP values. These correspond to the longitudes of the tangent directions to the Sagittarius spiral arm near $\ell \sim 50°$, and to the Scutum arm, or long bar, end (Benjamin et al. 2005) near $\ell \sim 30°$. One interpretation is that when viewing along a tangent direction, if the magnetic field direction follows the arm, then the plane-of-the-sky orientation projection changes rapidly with distance, leading to a dispersed pattern of polarizations and lower FP values. Whatever the correct interpretation for this behavior might be, the presence of a longitude-based change in FP that correlates with spiral arm properties shows that GPIPS stellar polarizations must be probing at least to the distance of the Sagittarius spiral arm and perhaps as far as the end of the long bar, some 7 kpc away.

3.4. Example Fields

As an exploration of the polarization properties for a variety of fields, five example fields were chosen from DR1 and are presented in Figures 8 through 12. They were chosen to sample the two FP minima with ℓ near the spiral tangent directions (fields GP645 and GP2843) and three directions corresponding to FP maxima with longitude, near $\ell \sim 54$, 34, and 20° (GP3077, GP1366, and GP182). Figure 8 (GP182; $\ell \sim 20°$) shows the combined H-band image obtained from the 96 images obtained in the 6 dithers and 16 HWP angles toward this field, overlaid with black vectors conveying the linear polarization percentage via their lengths (with a 2% reference vector in lower left) and polarization position angles via their orientations. The polarizations displayed show either detected polarization S/N (P/σ_P) at or exceeding 2.5, or were considered "significant upper limits" by having $\sigma_P < 1\%$ and are indicated by open circles. The direction parallel to the Galactic plane runs diagonally from lower right to upper left across this equatorially oriented field. These strong polarizations (mean of about 3%–4%) show very little departure in orientation away from the Galactic plane.

The next field, GP645 ($\ell \sim 26°$; Figure 9), shows nearly the same number of stars and stellar density, but far fewer polarization values were significantly detected. Also the position angles for the detected polarizations show either a lack of a coherent pattern, or an overlap of several coherent patterns that are oblique to each other. That the FP value for this field is low is clearly due to a lack of the directional coherence that is so prominent in the previous figure.

The third field, GP1366 ($\ell \sim 34°$; Figure 10), is drawn from the middle longitude maximum of FP versus longitude. Although showing many fewer polarizations than in the GP182 field, the vectors here are very well aligned with each other. However, the direction parallel the Galactic plane passes through this field with about the same orientation as for GP182, revealing that the magnetic field in GP1366, though coherent, is *perpendicular* to the Galactic plane. The data in DR1 may help answer whether such orientations are rare or common, but developing a final answer will likely require the full GPIPS data set to delineate the locations and properties of the misaligned regions.

The fourth field, GP2843 ($\ell \sim 51°$; Figure 11), is along the tangent to the Sagittarius spiral arm, and again shows few detectable polarizations and a lack of orientation angle coherence. Some vectors look to be aligned with the Galactic

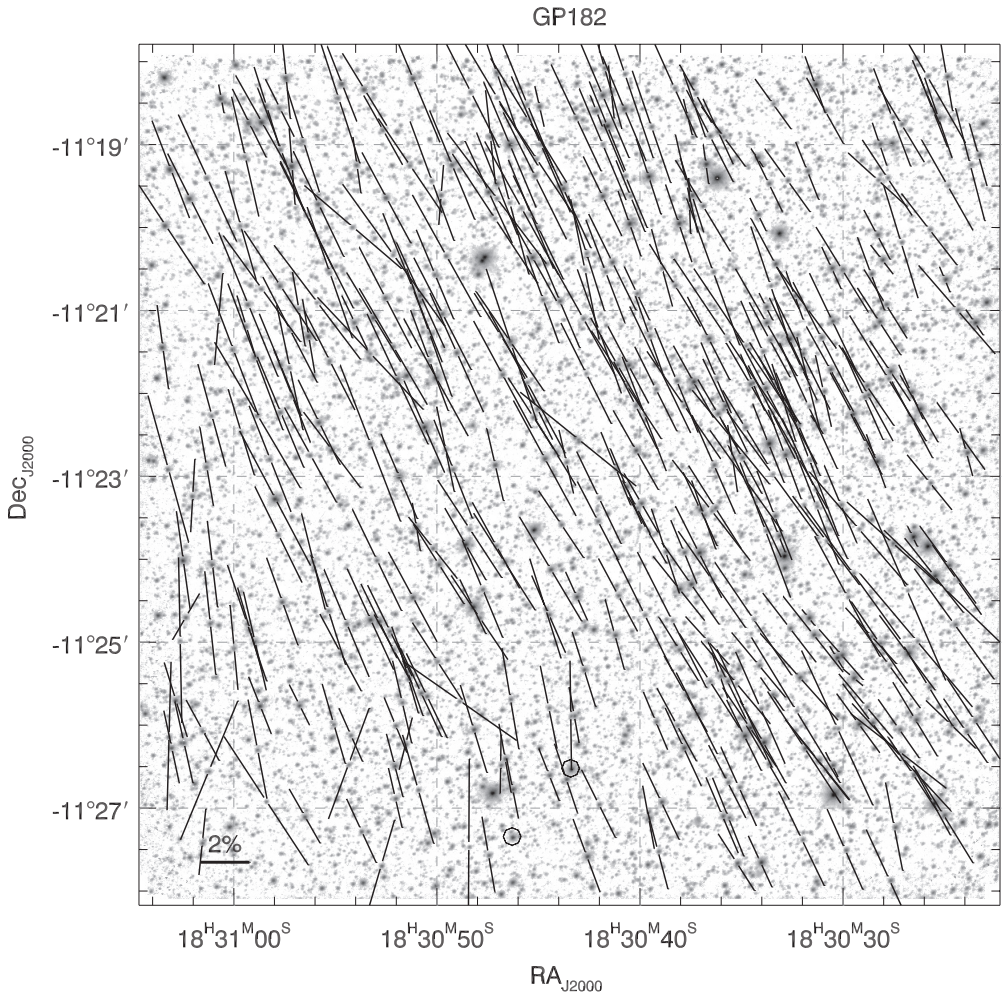

Figure 8. GPIPS field GP182 ($\ell = 20\overset{\circ}{.}457$, $b = -0\overset{\circ}{.}645$). Gray-scale image is the combined H-band photometry image. Polarizations for significantly detected stars (polarization S/N $\geqslant 2.5$) are shown as black vectors centered on their stars. Vector lengths represent percentage linear polarization—a 2% reference bar is shown in lower left. Vector orientations represent polarization position angles. Significant upper limits are shown as open circles.

plane direction, others are orthogonal, and still others are oblique to both.

The final field, GP3077 ($\ell \sim 54°$; Figure 12), is along another FP maximum, and does demonstrate a high degree of orientation angle coherence, though this time in a mostly north–south direction. At a more subtle level, there appears to be a left–right gradient in the percentage polarization (vector length) and a weaker divergence of vector directions for the upper-left and upper-right portions of the field.

4. STELLAR PROPERTIES

The contents of the DR1 data products were examined for their stellar properties, including photometric behaviors, key polarimetric trends, and reddening-based correlations.

4.1. Photometry and PHOTCATs

For each observed GPIPS field, the 96 (up to 117) individual images comprising a polarimetric observation were astrometrically registered, scaled, and combined to yield a "deep" photometric image (seen in Figures 8–12). These images were used to detect stars and measure their instrumental brightnesses. Stars detected in the deep images were matched to 2MASS (Skrutskie et al. 2006) point sources to determine the mean H-band offsets to apply to the Mimir-detections for each field in order to develop the PHOTCAT files of deep GPIPS photometry (see the Appendix). Paper I showed that the differences between Mimir and 2MASS stellar magnitudes calibrated in this fashion showed no average trend with faintness to the sensitivity limit of 2MASS.

Figure 13 extends that comparison to an examination of the difference magnitudes as a function of apparent stellar color, as measured by 2MASS in the J and K bands. In the figure, the 0.33 million DR1 stars with propagated GPIPS minus 2MASS H-band magnitude uncertainties $\sigma_{\Delta H}$ less than 0.1 mag are shown in the lowest panel, the 0.72 million stars with $\sigma_{\Delta H}$ between 0.1 and 0.2 in the middle panel, and the 62,000 stars with $\sigma_{\Delta H}$ between 0.2 and 0.3 in the upper panel. The bottom panel stars have the lowest uncertainties, are the brightest, and show the widest range of $(J-K)$ colors, signifying a wide range of extinctions probed, with little to no mean shift in the H-band difference magnitudes, though showing scatter consistent with the 45 mmag external uncertainty introduced earlier. This also holds for the middle panel, of less bright stars, though these do not probe to the same reddest colors, likely because extinction has dropped the reddest below detection by 2MASS in one or more band. The faintest stars, those in the upper panel, show an even more restricted range of colors but also show a small mean vertical offset of about 0.15 mag. This indicates a small brightness-dependent calibration difference between 2MASS

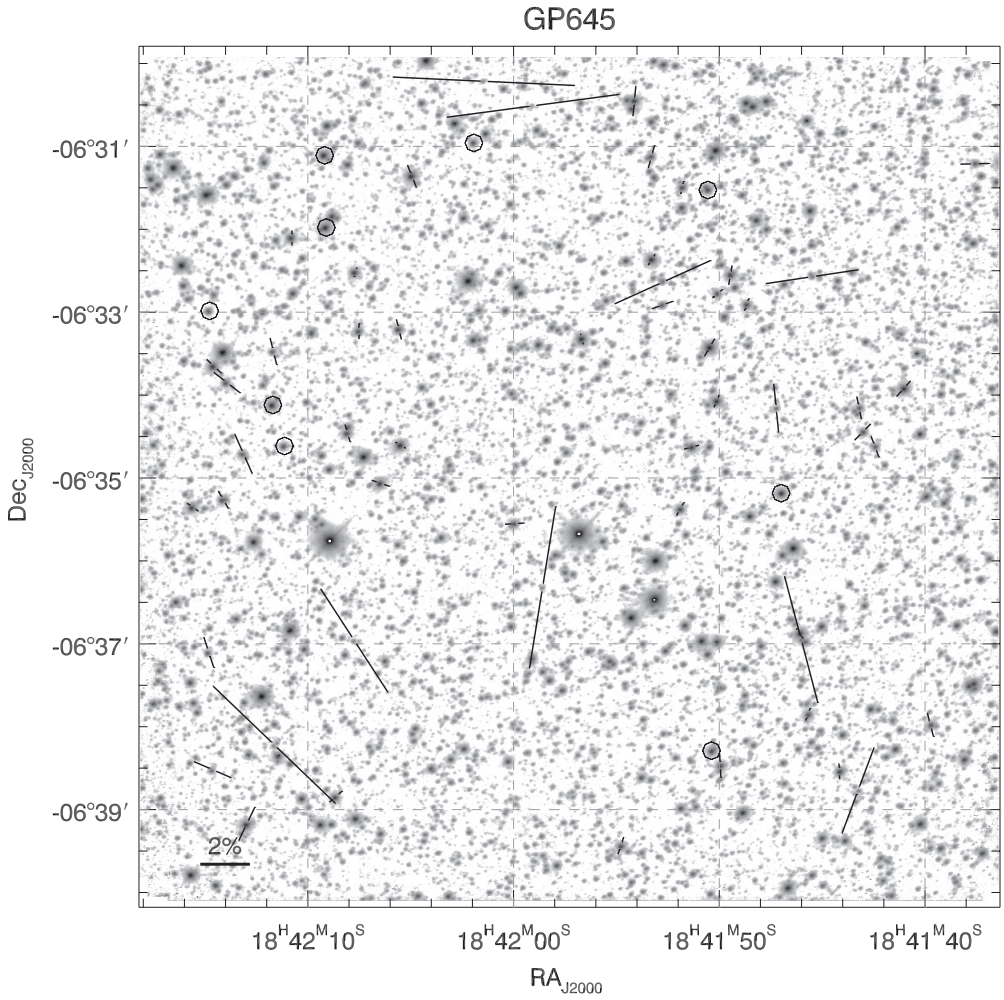

Figure 9. GPIPS field GP645 ($\ell = 25\overset{\circ}{.}995$, $b = -0\overset{\circ}{.}900$). See Figure 8 for image and vector descriptions.

and GPIPS and especially should be recognized when using GPIPS PHOTCAT magnitudes below the 2MASS point source limits in comparison to other catalogs.

The brightness distribution of PHOTCAT-cataloged stars for GPIPS DR1 is shown in Figure 14. There, the log of the average density of stars per GPIPS field (of angular size 10 × 10 arcmin) is shown as a function of the PHOTCAT *H*-band magnitude. Stars with magnitudes as bright and as faint as 6.5 and 17, respectively, are present. Also shown for comparison is the similar distribution of PHOTCAT DR1 stars that positionally matched to 2MASS stars. The faintness limit of 2MASS is seen as the early departure of the gray curve from the uniform rise of the black all-GPIPS curve. The cumulative distribution functions for both the all-GPIPS and 2MASS-matched GPIPS stars are shown as black-dashed and gray-dotted curves, referenced to the right-hand scale. Completeness holds until those curves depart from their steady rises to fainter magnitudes. This happens around 13th for the 2MASS-matched subset and 14th for the all-GPIPS DR1 PHOTCAT sample. The behavior in this figure has been effectively averaged over all 559 DR1 fields, so the effects of extinction and reddening should also be recognized to be present.

The PHOTCAT stars are mostly extincted normal stars, as shown in the NIR color–color distribution of Figure 15. There, the 2MASS $(J - H)$ and $(H - K)$ colors are plotted for the stars in PHOTCATs that match to 2MASS stars and for which the propagated color uncertainties are no larger than 0.15 mag.

4.2. Polarimetry and POLCATs

Characterization of the natures of the stellar entries in the POLCATs (Paper I) data products begin with a look at the behavior of polarimetric uncertainty with apparent magnitude, moves to comparing the color–color distribution of the polarization-detected stars to the same plot for PHOTCAT stars, examines the polarization histograms as a function of S/N, and provides some interpretation to aid users regarding what to expect, and be concerned about, when using the GPIPS data products.

The uncertainties in the linear polarization percentages σ_P for the POLCAT DR1 entries contain the propagated effects of the scatter in the redundantly measured IPPA stellar brightnesses used to compute the four Stokes *Q* and *U* values from the photometry developed from the 16 HWP images as well as components from the instrumental polarization corrections and the polarization efficiency uncertainties (Papers 1 and 2). Similarly, the polarization position angle uncertainties contain the effects of all these as well as the uncertainty in the HWP instrument offset angle calibration for each observing run (Paper II).

However, no S/N or magnitude cuts were applied to the flow of stellar data through the software pipelines into the POLCATs data products. Hence, most POLCAT stellar entries do *not* represent polarization detections nor significant upper

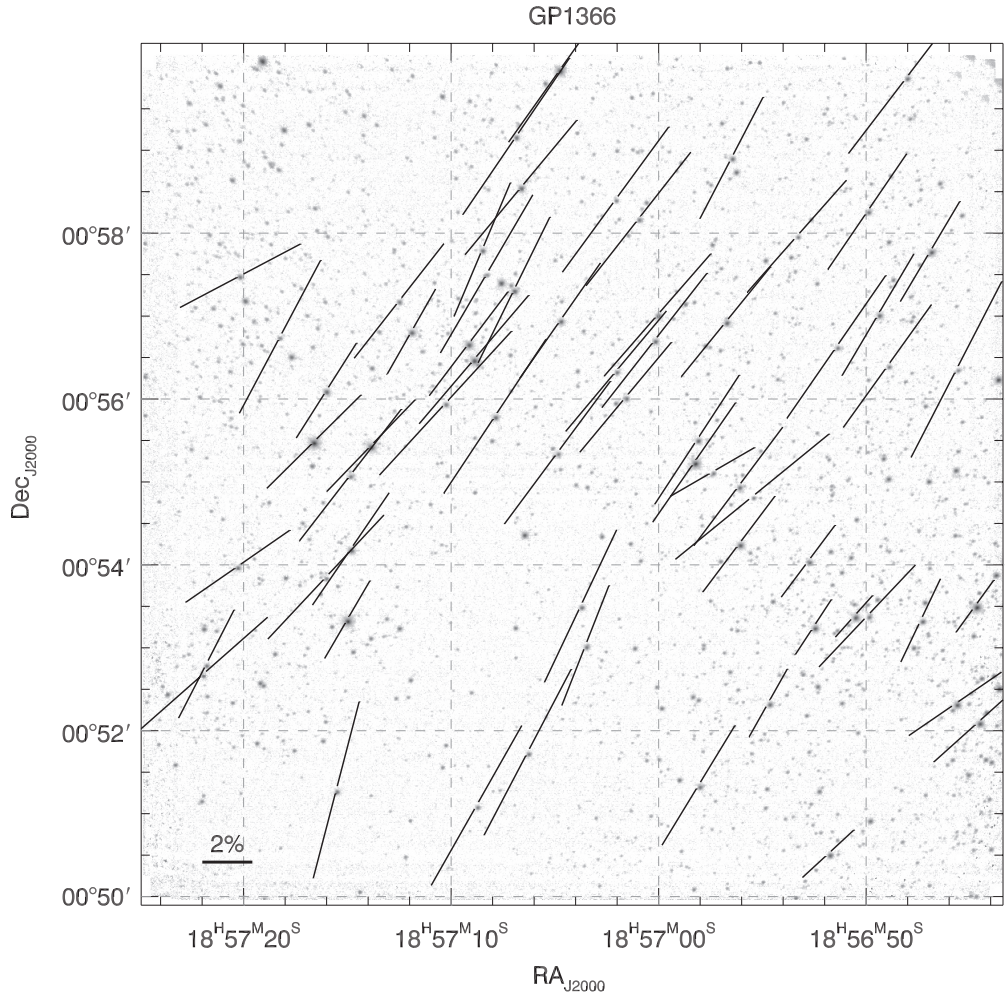

Figure 10. GPIPS field GP1366 ($\ell = 34.^{\circ}392$, $b = -0.^{\circ}834$). See Figure 8 for image and vector descriptions.

limits, but instead have high Stokes Q and U uncertainties due to having too few detected stellar photons. Nevertheless, because Stokes Q and U are Gaussian-distributed quantities, these (polarization) non-detected stars can still yield useful science, as described in later sections. Most users of GPIPS POLCATs will, however, be interested in the properties of the stars showing significant polarization detections or exhibiting significantly low upper limits. However, because polarization S/N is based on ratios of non-Gaussian-distributed quantities, S/N alone is not a sufficient selection criterion. High apparent polarization values can lead to high S/N even for unusually high σ_P values and such fluctuations to high P values seem to increase with stellar faintness.

4.2.1. Stellar Polarization Subsets by Usage Flag Value

In the POLCATs data products, a Usage Flag (UF) value is included to provide a rough classification for data entries, as explored in Figure 16 and summarized by number in Table 2. The figure shows the behavior of POLCAT stars in the σ_P versus m_H plane, as contours of apparent stellar density. The contours start from 90% of the peak density and drop by a factor of two between each nested contour. Three zones are delineated and identify the three possible values of UF assigned.

The UF = 1 zone is bounded by stars showing σ_P of 2% and m_H of 12.5 mag. The UF = 1 stars are those POLCAT entries most likely to be useful for direct magnetic field mapping using individual star polarization values.

Surrounding it is the UF = 2 zone, which goes out to σ_P of 10% and m_H of 14 mag. These stars, suitably averaged in U and Q over solid angle, are capable of returning low angular resolution magnetic field maps and of revealing fields to greater distances than for many of the UF = 1 stars. However, given the mean polarizations seen in the UF = 1 stars (see below), few of the UF = 2 stars will individually exhibit adequate S/N values to constrain magnetic field orientation angles. For UF = 2 stars, averaging of multiple star values will be the key that unlocks useful polarimetric and magnetic field information.

Table 2
DR1 Stellar Samples

Stellar	All Stars		Stars with 2MASS Colors	
Sample	Number	Fraction	Number	Fraction of All
(1)	(2)	(3)	(4)	(5)
UF = 1	177, 130	16.9%	167,017	94.3%
Subset *UF = 0* [a]	*50,303*	*4.7%*	*47,861*	*95.1%*
UF = 2	430,597	41.1%	332,521	77.2%
UF = 3	441,003	42.0%	172,981	39.2%
Totals	1,048,730		672,519	

Note. [a] A subset of the UF = 1 sample, selected for $(P/\sigma_P) > 2.5$, so not included in totals.

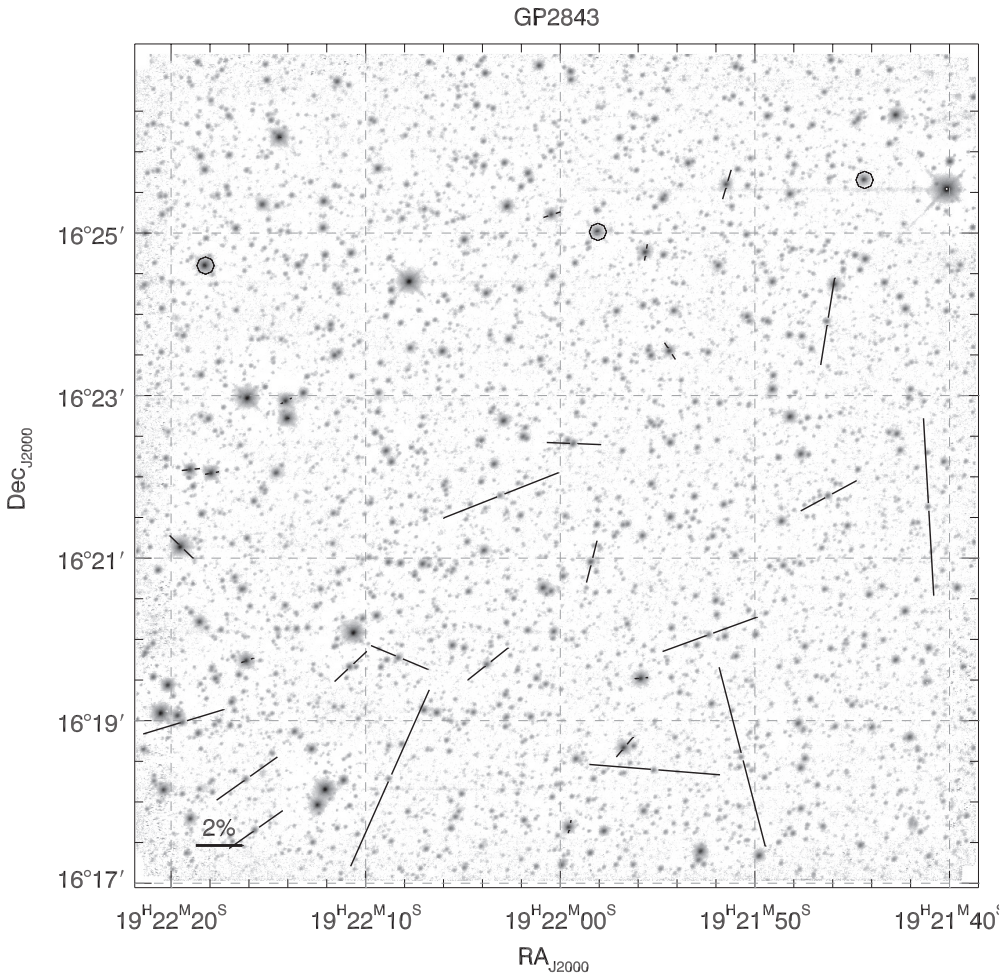

Figure 11. GPIPS field GP2843 ($\ell = 50\overset{\circ}{.}933$, $b = +0\overset{\circ}{.}857$). See Figure 8 for image and vector descriptions.

Finally, the remaining stars are given the UF = 3 flag, including those with σ_P values as high as 100%. Only the coarsest of averaging, over hundreds to thousands of UF = 3 stars, will reveal magnetic field orientation information. However, the huge number of these stars offers the potential for testing interesting astrophysics via large-scale averaging, structure functions, and other statistical tools, as demonstrated in later sections.

Because of the utility of UF = 1 stars for direct magnetic field orientation mapping, of the UF = 2 stars for angle-averaged deep magnetic field mapping, and of the UF = 3 stars for revealing the power spectrum of magnetic field fluctuations and structure over large length and angular scales, all of these stars are included in the POLCATs data products.

Figure 16 shows that the dominant behavior of higher polarimetric uncertainties for fainter stars is due to Poisson noise (photon starvation and background noise for the faint stars). Much weaker effects are seen in the swing to higher σ_P values near 7th mag and the faint, asymmetric wing to brighter magnitudes for σ_P values in the 2%–20% range. The calibration floor of about 0.1% for single observations (Paper II) is met around 8th mag. The overall well-behaved nature of the great majority of the stars reflects the conservative approach to culling bad data and the attention to full inclusion and propagation of all sources of uncertainty.

The approximate angular sky sampling achieved by the entries in the POLCATs products is summarized in Figure 17. This figure uses all of the DR1 data, normalized by the number of DR1 fields, to explore the average density of stars per field as a function of stellar magnitude. The UF = 1 sample has its greatest stellar density very near its magnitude limit of 12.5, reaching about 40 stars per 0.2 dex of mag per 10×10 arcmin of field size. The dashed lines show the cumulative stellar densities brighter than a given magnitude, and are more appropriate for sampling or angular resolution determinations. Labeled horizontal black dashed lines identify some key stellar density milestones. The UF = 1 cumulative distribution reaches a mean stellar density of one star per 2×2 arcmin square box by 9th mag and achieves average sampling of 30–45 arcsec between stars for the full UF = 1 sample, which is somewhat better than reported in Paper I for a 16-field subset.

As noted above, the UF = 2 and UF = 3 samples have different purposes than the UF = 1 sample. The density mark at 800 stars per 10×10 arcmin shows an example brightness level of stars that could be included to form one average polarization value per GPIPS field, using only UF = 2 entries. In doing so, if the mean σ_P for those stars is 8%–10% (see the previous figure), then averaging will return a new σ_P closer to 0.3%, which is low enough to achieve good polarimetric S/N even for $P \sim 1\%$. Similarly, for the UF = 3 case, binning to one degree resolution nets more than 50,000 stars per bin, reducing even 100% mean σ_P values to under 0.5%. These stars will have H-band magnitudes of about 14–15th, and may probe to great distances. These UF = 2 and UF = 3 stars, when binned,

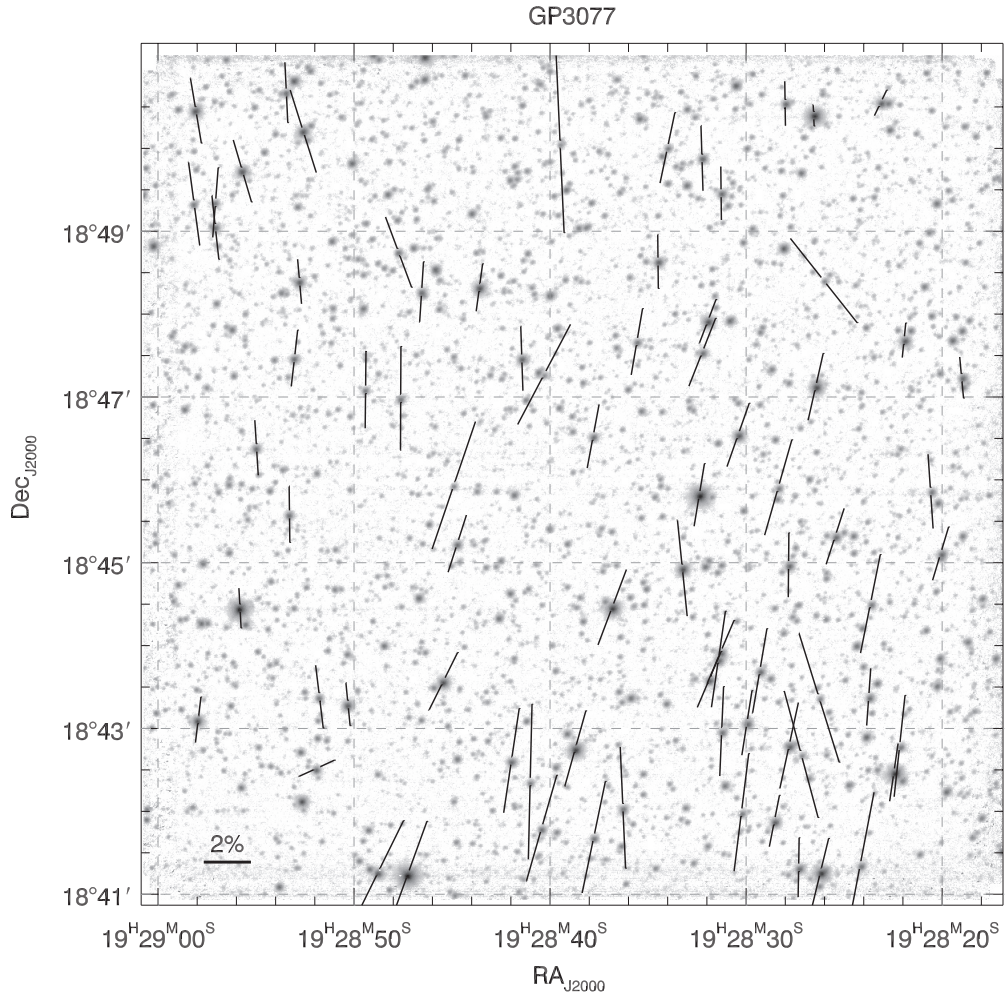

Figure 12. GPIPS field GP3077 ($\ell = 53.^{\circ}796$, $b = +0.^{\circ}601$). See Figure 8 for image and vector descriptions.

may reveal magnetic field information that the UF = 1 stars cannot.

The distributions of polarization values measured for the three UF samples are shown in Figure 18. In constructing this figure, all POLCAT polarizations below 0.3% (i.e., all upper limits and most non-detections) were excluded. Each UF distribution was normalized by the total polarization-detected stars in each UF group. The UF = 1 distribution peaks at about 1% polarization, the UF = 2 curve at about 3%, and the UF = 3 curve at about 10%. Cumulative distributions were computed from these relative ones and are also plotted in the figure. Median values of 1.45%, 4.25%, and 13.85% P were found for the UF = 1, 2, and 3 samples, respectively. The UF = 1 sample shows a fairly narrow range of typical polarizations, with 25th and 75th quartile values of the cumulative distribution at 0.85% and 2.25%, respectively. That the median UF = 1 polarization is only of the order of one percent underscores the importance of maintaining calibration of the instrument to ∼0.1% and of careful attention to an observing scheme and data reduction and analysis steps that preserve precision.

4.2.2. Reddening and Polarization

The NIR colors of the stars contained in the POLCATs are nearly the same as the colors seen in the PHOTCATs (Figure 15). To explore the remaining small differences, an image representing the stellar density in the $(J - H)$ versus $(H - K)$ color–color plane was developed for the PHOTCAT stars, again for color uncertainties no larger than 0.15 mag. A similar image was developed using entries in the POLCATs. Each image was normalized by the total number of stars in the image and a difference image was formed. This was normalized by the maximum value found in the larger of the two input normalized images. The resulting image of relative color–color distribution differences is shown in Figure 19. The orange filled contours identify the portion of the image for which the POLCAT stars have higher relative densities in the color–color plane than do the PHOTCAT stars. The blue filled contours identify the zone having a deficit of POLCAT stars, in a relative sense. The maximum range of excess is up to about one percent, as is the range for the deficit zone. The white lines originating from zero show the Bessell & Brett (1988) loci of unextincted dwarf colors (lower curve) and unextincted giant colors (upper curve). The reddening vector is parallel to the direction of the elongation of the orange contours.

An interpretation of this relative difference diagram is that POLCAT entries contain a slight deficit of unextincted giant and dwarf stars—those along the portion of the white curve prior to bifurcation and also along the lower, dwarf, branch. The POLCATs also have a slight deficit of extincted dwarfs—those that lie off the lower white curve but run up a reddening line parallel to the direction of the orange contour elongations. This is

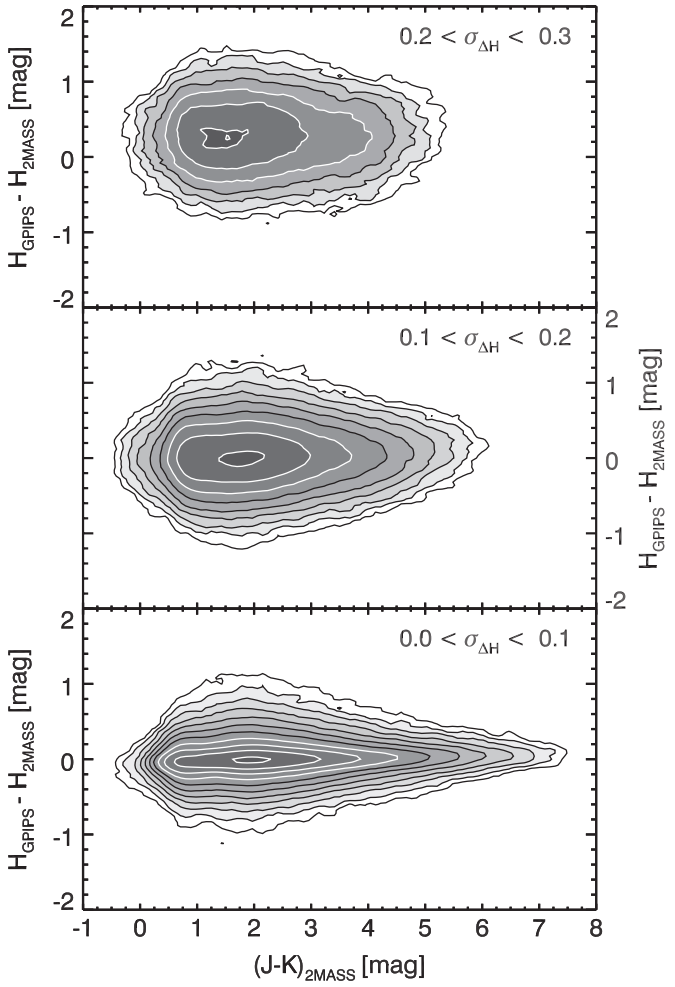

Figure 13. Comparisons of H-band magnitudes for GPIPS DR1 and 2MASS vs. 2MASS $(J - K)$ color. Bottom panel: stars selected for uncertainties in their H-band difference magnitudes of less than 0.1 mag. Middle panel: stars with uncertainties between 0.1 and 0.2 mag. Top panel: stars with uncertainties between 0.2 and 0.3 mag. Brightest stars are in the bottom panel; the faintest are in the top panel. Central contours represents 90% of peak stellar density in each panel and subsequent contours drop by a factor of two. Note the weak vertical offset in the top panel and its absence in the middle and bottom panels.

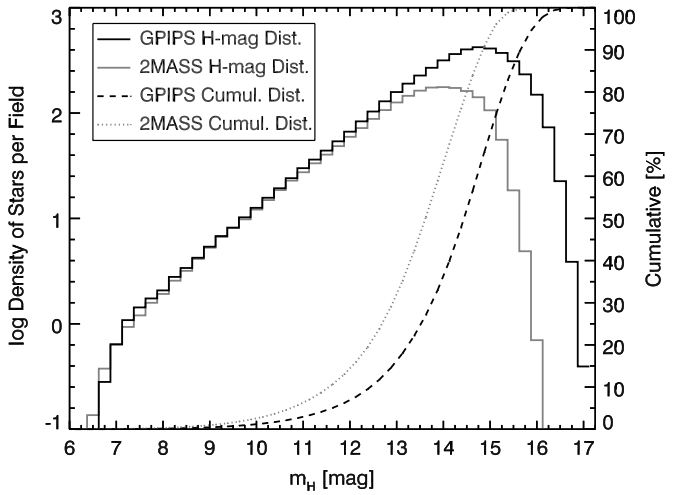

Figure 14. Magnitude distributions of all GPIPS DR1 PHOTCAT H-band stars (black histogram) and those matching to 2MASS stars (gray histogram). Also shown are the cumulative distribution functions, with scale at right. The PHOTCAT stars begin to depart from completeness beyond 14th mag and show an increasing rate of failure to match to 2MASS stars beyond 13th. About half of the GPIPS stars have magnitudes brighter than about 14.3 mag.

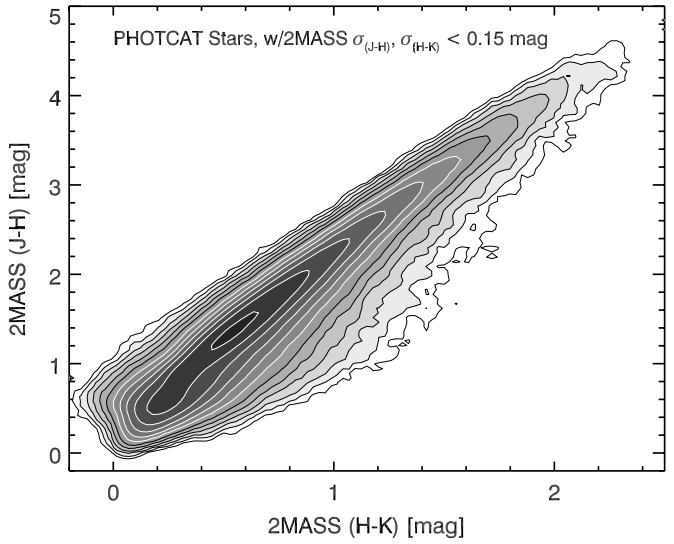

Figure 15. Near-infrared color–color distribution of GPIPS DR1 PHOTCAT stars with matching 2MASS colors and for which the color uncertainties are no larger than 0.15 mag. The central contour represents 90% of the peak stellar density and subsequent contours decrease by factors of two. Most stars are reddened normal dwarfs or giants, though a small fraction of stars do show some color excess by departing from the reddening line along the $(H - K)$ axis.

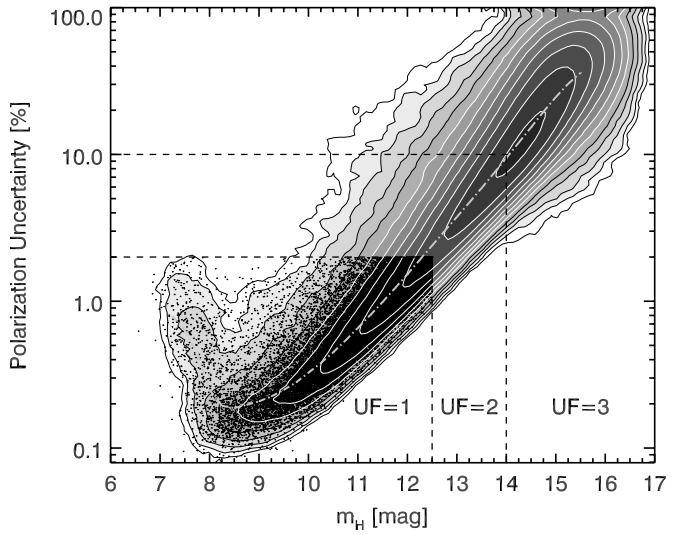

Figure 16. Uncertainty of linear polarization percentage σ_P for GPIPS DR1 POLCAT stars vs. their H-band stellar magnitudes m_H. Shown are filled contours from 90% to 0.044% of the maximum of stellar density, scaled by a factor of two between steps. The three Usage Flag (UF) regions are identified, as described in the text. In the UF = 1 zone, every fifth star has also been plotted as a black dot. A dot-dashed gray curve traces the run of mean values of σ_P, computed for each 0.25 mag wide band of m_H.

not surprising, as detection of H-band polarization requires some minimum column of dust to yield detectable dichroic extinction. Unextincted stars foreground to any such dust should show no polarization. That the same deficit should follow the extincted dwarfs is more curious, but may be due to sensitivity limits. The PHOTCATs probe to some three magnitudes fainter (16 times deeper) than the individual HWP images, so the PHOTCATs may contain extincted dwarfs below the sensitivity limit of the POLCATs. All of the dwarfs in the reddened portion of the blue contours are quite late M-type, and intrinsically faint, so even modest extinction is likely enough to cause them to be missed in the POLCATs.

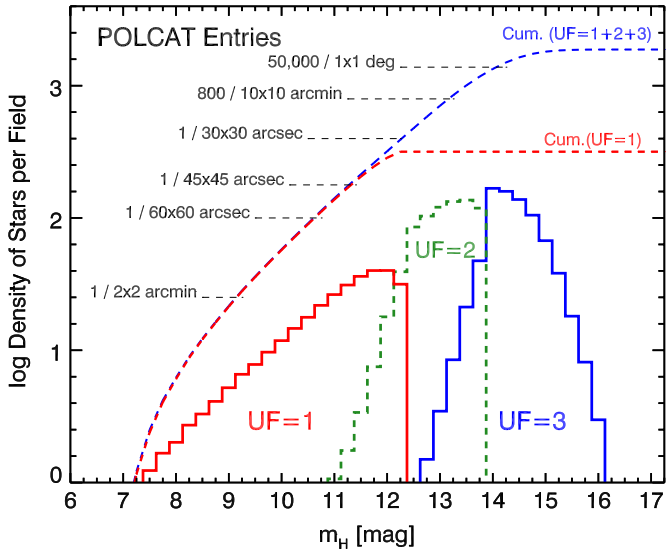

Figure 17. Log of the average density of GPIPS POLCAT stars per 10 × 10 arcmin field in DR1 as a function of *H*-band magnitude, colored by UF values (red for UF = 1, green for UF = 2, and blue for UF = 3). Dashed curves show cumulative stellar densities brighter than a given *H*-band magnitude. Some important stellar density values are labeled—these are described in Section 4.2.1. Note that the UF = 1 and UF = 2 samples have fixed faint magnitude limits (see the previous figure), so their sharp cutoffs are not related to completeness. The average density of POLCAT entries (all UF values) is about 1,700 stars per field.

(A color version of this figure is available in the online journal.)

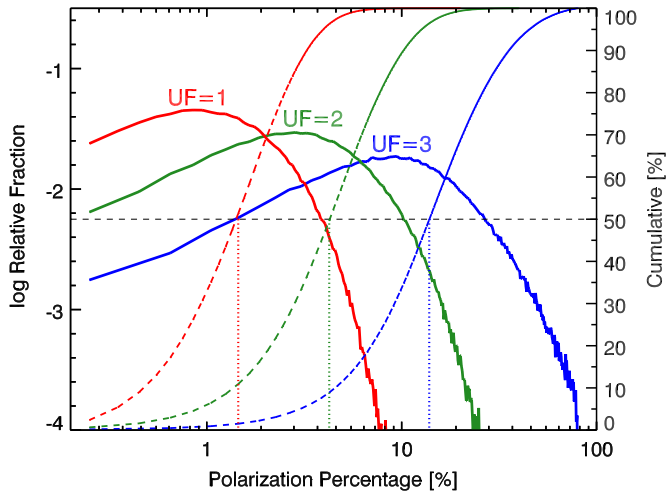

Figure 18. Relative distribution functions of percentage polarization P for the three UF stellar sample designations (solid red, green, blue curves). Cumulative distribution functions, using right-hand vertical scale, are shown as partially dashed colored curves. Median values for each sample are shown by vertical dotted lines, in the three colors.

(A color version of this figure is available in the online journal.)

POLCATs instead are weakly biased to favor extincted giants compared to the PHOTCATs. However, both the deficit and the excess are not strong effects, and the full color–color distributions for POLCATs and PHOTCATs are remarkably similar.

The measured polarizations were also examined for their dependence on apparent stellar color, which is a proxy for dust reddening, in Figure 20. In the top (UF = 1) panel, the highest-quality polarizations show the expected behavior of correlated dust reddening and polarization, namely along a slope of about 2% P_H per mag of $(H - K)$, while remaining mostly below the (dashed) maximum polarization line (Whittet 2003). This locus of maximum polarization was found by Serkowski et al. (1975),

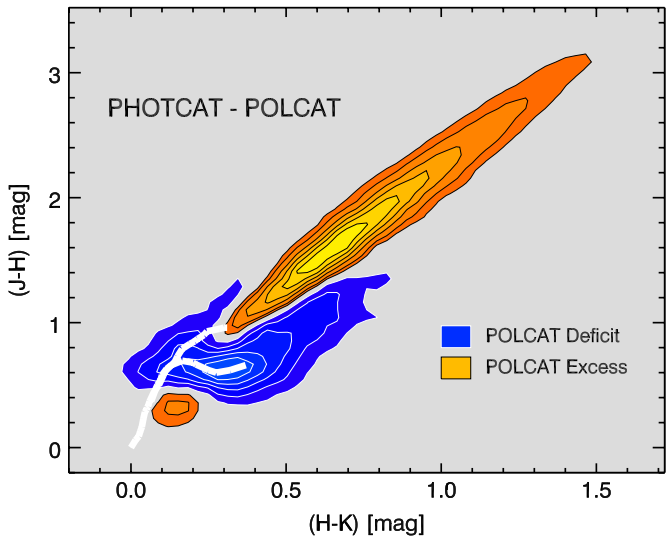

Figure 19. Relative color–color difference diagram computed from the scaled difference of the PHOTCAT color–color distribution and the POLCAT color–color distribution. The orange filled contour zones delineate the portion of the diagram showing up to about a one percent excess of the fraction of stars with polarization entries in the POLCAT, relative to the photometric-only entries in the PHOTCAT. The blue filled contour zones identify the region with up to about one percent deficit in the POLCAT stellar color–color distribution. Overlaid as thick, white curves are the Bessell & Brett (1988) loci for unextincted dwarfs (lower curve) and giants (upper curve). The POLCAT shows a deficit of unextincted dwarfs and giants as well as extincted late-type dwarfs, making up for this with a higher relative fraction of extincted giants.

(A color version of this figure is available in the online journal.)

and interpreted using the optical properties of anisotropic dust grains perfectly aligned with the local magnetic field by Jones (1989) and Jones et al. (1992). Here, the Serkowski et al. line has been scaled to *H*-band and $E(H - K)$ assuming a Serkowski Law (Serkowski et al. 1975; Wilking et al. 1980) behavior of polarization with wavelength and the extinction law of Rieke & Lebofsky (1985).

Stars of nearly all spectral types show a narrow range of intrinsic $(H - K)$ colors (Bessell & Brett 1988; Figure 19), so that apparent $(H - K)$ values beyond this range are good tracers of dust reddening. In the top panel of Figure 20, the reddenings extend out to $(H - K) \sim 2$, or $A_V \sim 20$–25 mag and the polarizations extend up to about 6%. In contrast, the bottom (UF = 3) panel shows most of the stars above the maximum ISM polarization line and reddenings to only half the value of the UF = 1 maximum. There is a partial, weak correlation of reddening and polarization for some of these UF = 3 stars, as expected for their photon-starved (noise dominated) natures. The middle panel (UF = 2) stars show a mixture of behaviors drawn from the high-quality UF = 1 stars and the high-noise UF = 3 stars. In the UF = 2 panel, about half of the stars appear below the ISM polarization limit, and show polarization and reddening correlated. But about half appear above the limit line, likely due to higher polarimetric uncertainties. These distributions confirm that the UF = 1 subsample will be best for direct magnetic field mapping and characterizations, using individual stars, and that the UF = 2 and UF = 3 subsamples can return magnetic field information if suitably averaged or analyzed in bulk.

4.3. Young Stellar Objects

Disks and envelopes around young stellar objects (YSOs) could be a significant source of scattered *H*-band light (Casali

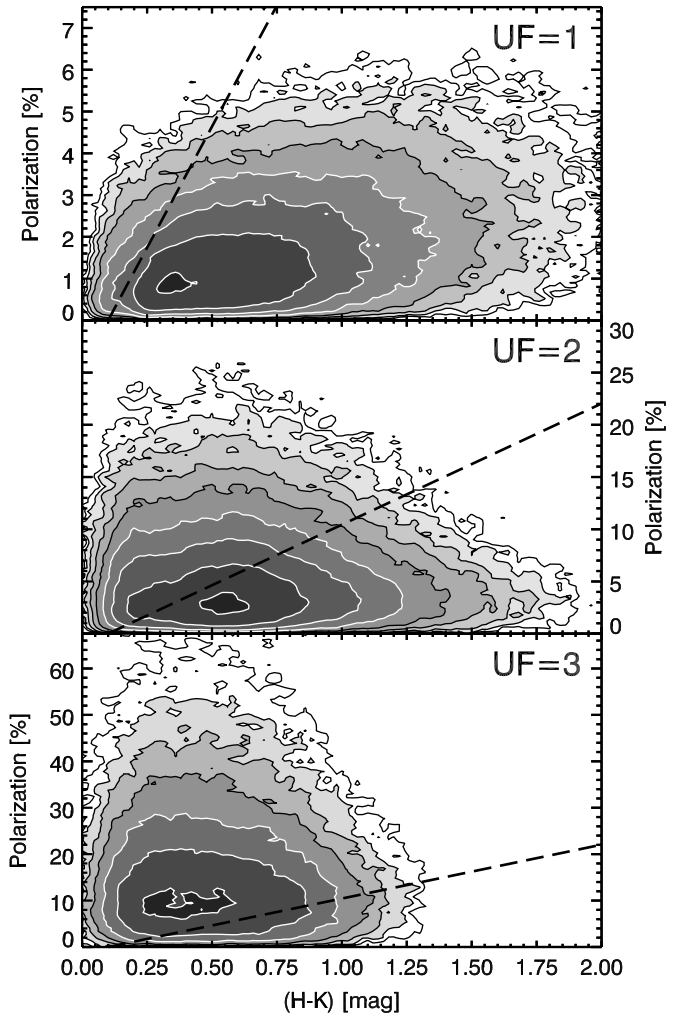

Figure 20. DR1 H-band polarization percentage P vs. 2MASS $(H-K)$ stellar color, for the three UF subsamples. Each panel shows filled contours of the relative density of stars, starting from 90% of the maximum and decreasing by a factor of two for each successive contour level. The dashed lines show the loci of maximum interstellar polarization for perfect grain alignment, inferred from optical values and scaled to H band. See discussion in text for interpretation of these distributions. Note the different scales of the vertical axes.

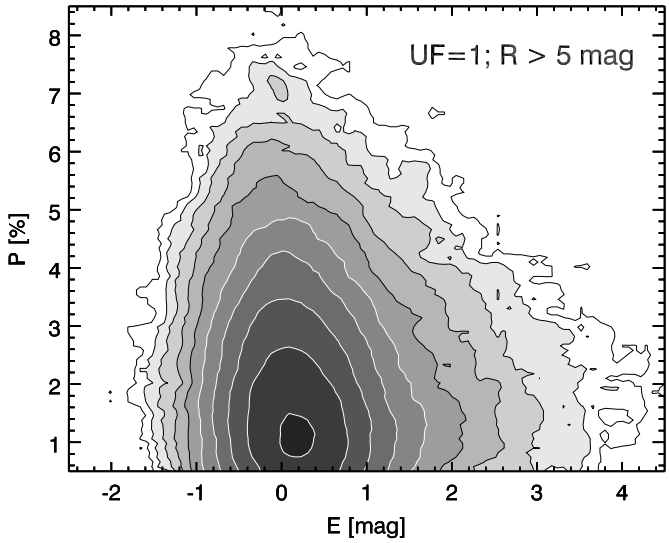

Figure 21. Stellar polarization percentage P vs. synthetic excess E measure, shown as filled contours of stellar density, for the stars in the UF = 1 sample of DR1 showing synthetic reddening R values exceeding 5 mag. The central contour represents 90% of the maximum stellar density and subsequent contours are each one-half of the previous value. The majority of the stars have E values near zero, with an FWHM E width of about unity. The most reddened normal stars show polarizations up to about 8% near E of zero. A second population of stars showing polarizations up to about 4% and significantly positive E values is not mirrored at negative E.

1995; Sogawa et al. 1997; Simpson et al. 2009) leading to polarization detections that are unrelated to magnetic fields in the intervening ISM. A detailed study of YSOs in the GPIPS region is beyond the scope of this paper, but an examination for their presence and assessment of the degree to which YSOs might contaminate magnetic field interpretations was conducted.

YSOs, and disks, are often revealed in NIR color–color diagrams via their color excesses, primarily at the longer wavelengths (K and L bands; Meyer et al. 1997; Lada et al. 2000) as redward departures of some of the stars from the normal reddening distribution along the $(H-K)$ axis. Using the highest-quality, UF = 1 stellar sample, the $(J-H)$ versus $(H-K)$ distribution (already shown to be very similar to the distribution in Figure 15) was remapped, as follows. The slope of the dominant, reddened stellar distribution was measured and used to rescale the $(J-H)$ axis to create an $(H-K)$-like scaling. Next, both axes were further scaled by the dense cloud value of 12.5 to convert $E(H-K)$ to A_V (Whittet 2003).

In this remapped space, both axes have similar units (of A_V) and the reddened locus of stars falls at about unity slope, though there is some curvature at the high reddening end and a strong turn-up at the low reddening end due to the presence of unreddened dwarf stars. A new pair of 45° rotated axes was introduced such that stars exhibited reddening along one axis (a "Reddening" axis R) and exhibited NIR excess perpendicular to the reddening axis (along a new "Excess" axis E). This approach is similar to the use of both $(J-H)$ and $(H-K)$ in computing extinctions for the "NICER" method (Lombardi & Alves 2001), but extends it by following the deviation of stars away from the reddening axis along the new E axis. The zero of the E axis was set through use of the locus of reddened stars as the zero reference, under the assumption that most of the scatter of E values close to the distribution center was due to a mixture of stellar types and 2MASS photometric uncertainties. The zero of R was based on the mean $(H-K)$ unextincted stellar color of 0.15 mag (Lada et al. 1994), also mapped to $(J-H)$ via the reddening slope.

In this new space, both R and E have units of magnitudes, corresponding to A_V for the R axis and NIR excess for the E axis (albeit no longer along the old $(H-K)$ color direction). For the UF = 1 stars, subsamples were selected by binning in R and examining their polarizations as a function of excess E. The full range of R values, from about −3 to +30 mag, was examined, in bins with 5 mag widths. No strong differences were seen in the P versus E behavior as a function of R (not shown), though this should be re-examined when all of the GPIPS data are available.

As noted above, the stellar distribution in the E versus R plane is complex for $R < 5$ mag, where unextincted dwarfs and giants broaden the distribution perpendicular to the reddening direction (cf. Bessell & Brett 1988). Consequently, the stars showing $R > 5$ mag, those clearly affected by reddening and so most able to reveal magnetic field directions, were collected and are plotted in the P versus E diagram shown in Figure 21. There, base two logarithmic contours of relative stellar density reveal the polarization dependence on NIR excess. Two main

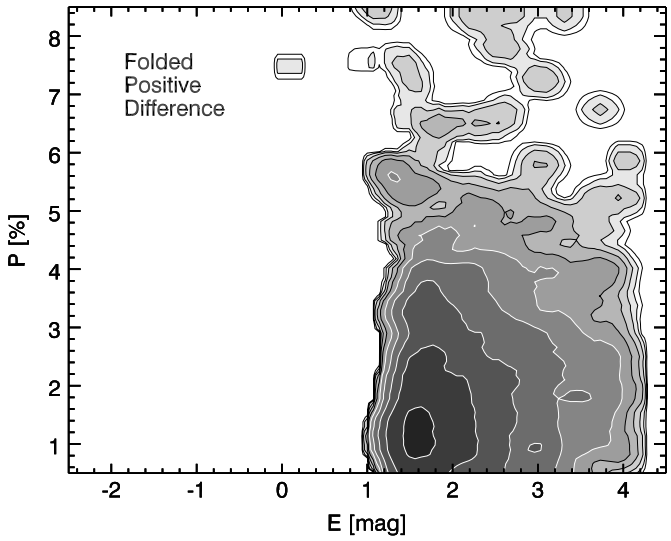

Figure 22. Stellar distribution of polarization P vs. excess E, after mirroring the distribution shown in Figure 21 and subtracting from the original distribution, to isolate the asymmetric portion of the distribution. Contours are stepped by half, from the central contour representing 90% of peak stellar density. This distribution contains about 2% of the stars seen in Figure 21. The highest density of stars is near $E = 1.5$ mag and $P = 1.5\%$, with some stars showing E values to 4 mag and P values up to about 6%. This potentially YSO-containing population does not show P values as large as for the reddened, $E \sim 0$, population.

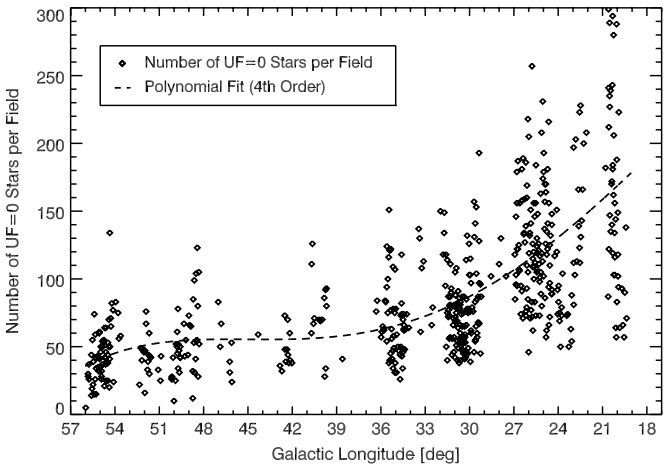

Figure 23. Number of high-quality, UF = 0, stellar polarizations detected per GPIPS field in DR1 as a function of Galactic longitude ℓ. The dashed curve is a fourth-order polynomial fit that reveals the increase in stellar counts as the Galaxy's central bulge begins to be sampled. This shows GPIPS polarizations probe deeply into the inner regions of the Galaxy, well beyond the nearest spiral arms. This figure should be compared to Figure 7 to see that the field polarization and numbers of stars detected are independent.

populations appear to be present. The first is centered about $E = 0$ and extends to polarizations of about 8%. The second central contour represents 45% of the peak density, and so is a fair representation of the FWHM extents along both axes. The width in E, of about 1 mag, is fully consistent with 2MASS photometric uncertainties of 0.05–0.1 mag for these stars. The polarization range far exceeds corresponding polarimetric uncertainties. The conclusion is that this population of stars shows reddening ($R > 5$ mag of A_V at minimum), no significant NIR excess, and is significantly polarized. This population is ideal for tracing magnetic fields.

A second population is also present, one which is seen to larger positive excess E values and yet extends to only about half of the polarization extent of the first population. In order to better isolate this second population from the first, a difference image was formed. To do so, the Figure 21 image of stellar density was reflected about $E = 0$ and subtracted from the original image to form Figure 22. This new distribution represents the positive excess revealed in this E-folded difference. It shows a population that has significant NIR excess ($E > +1$ mag). It is noteworthy that the P values for this population do not extended much beyond 4–6%. YSO disks and cavities, when resolved, show much higher NIR polarizations (up to 85%, Simpson et al. 2009). So, either GPIPS (DR1) data are not particularly sensitive to these highest polarization objects, or these objects rarely appear in a uniform areal survey.

The fraction of stars appearing in the stellar density distribution of Figure 22 is about 2% of those in Figure 21. This value represents a hard upper limit on the YSO contamination, for two reasons. First, some dwarf stars will receive enough reddening to appear in this excess population, though they have no bona fide excesses. This is a consequence of the locus of unreddened dwarf stars in NIR color–color space and the remapping into (R, E) space. Second, users of DR1 and GPIPS may use this remapping to select for the first, magnetically pure sample of stars based on their lack of significant E departures, to generate samples of stars showing only reddening with which to trace magnetic fields. Even if no such cleaning is performed, some 98% of the stars in DR1 are unlikely to be contaminated by the effects of YSOs or circumstellar disks.

5. SCIENCE TOOLS AND HIGHLIGHTS

Having established the UF = 1 subsample of DR1 as containing the highest quality polarization measurements for individual stars, a few science-based explorations were pursued to gain a better understanding of the nature and extent of the magnetic field probed in the Galactic disk. This began by further restricting the UF = 1 subsample to those stars exhibiting polarization S/N greater than 2.5 (corresponding to $\sigma_{\rm PA} < 11^\circ$). In keeping with standard astronomical practice, this new set of stellar polarizations was designated "UF = 0" to identify that it represents a subsample of UF = 1 stars whose data quality level is even further from the high uncertainty UF = 2 and 3 samples than is the UF = 1 sample (see Table 2).

5.1. Stellar Density versus Longitude

One revealing distribution was the number of UF = 0 stars detected per GPIPS field in DR1 versus Galactic longitude ℓ, shown in Figure 23. The individual fields show a wide range of densities of detected high-quality polarization stars, from a low of 5 to a high of 384 (clipped in the figure) and a systematic trend for more stars with decreasing ℓ. This is likely the result of increased numbers of cool giants associated with the Galactic bulge, and less likely due to star formation in the Galactic Ring or spiral arms. GPIPS polarizations are sensing the magnetic field in nearby spiral arms (see Figure 7), but are also probing to regions close to the center of the Galaxy where cool giant stars in the bulge dominate. A similar plot of stellar density versus Galactic latitude b (not shown) is mostly flat and featureless for the UF = 0 DR1 sample.

5.2. Mean Galactic Magnetic Field Direction

The polarization position angles measured toward the stars comprising the UF = 0 subsample are the best ones for tracing

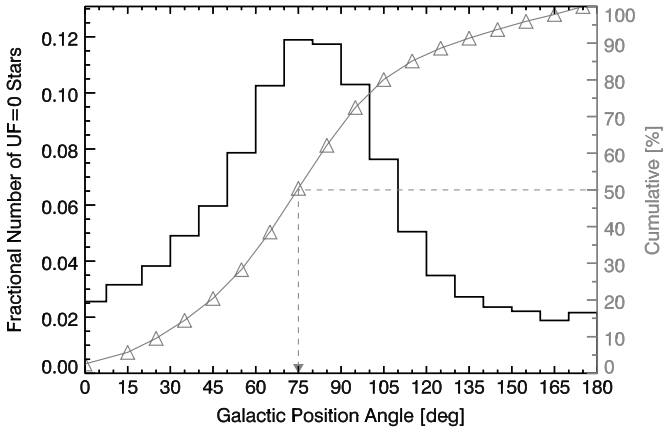

Figure 24. Histogram of Galactic position angles (GPAs) measured for the UF = 0 subsample of high-quality polarization detections. The histogram has been normalized to unity area for this subsample of over 50,000 stars. The cumulative distribution is shown as the gray curve. Median value of 75° is indicated by vertical arrow. A magnetic field oriented purely parallel to the Galactic disk would show GPA = 90°.

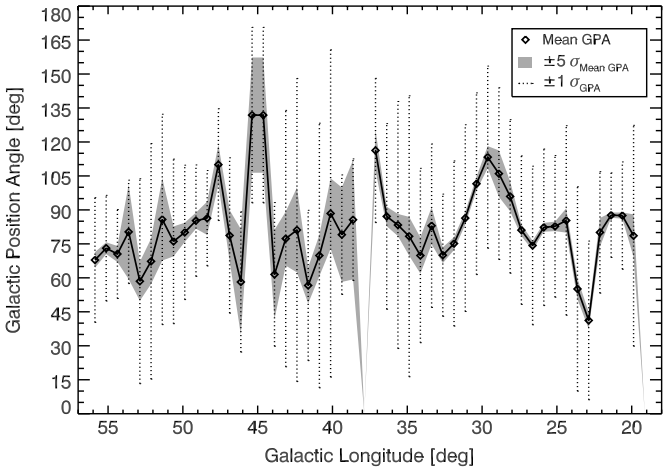

Figure 25. Mean Galactic position angle (GPA) vs. Galactic longitude ℓ for the UF = 0 subsample of high-quality polarization detections. Longitude bins of width 2.°75 are spaced by 0.°75. Connected open diamonds show (unweighted) mean GPA in each bin. Vertical dotted lines show bin content GPA dispersions ($\pm 1\sigma$), while the gray bands show ±5 times the uncertainties of the mean GPA values. Bins with no DR1 UF = 0 entries are present near $\ell = 38°$ and 19°. Significant deviations above and below GPA = 90° are present.

the directions of the Galactic magnetic field. The histogram of position angles in the Galactic system (Galactic position angle, GPA; which increases toward $+\ell$ from $+b$) is shown in Figure 24. Here, UF = 0 stars were binned by 10° of GPA and the entire distribution was normalized by the total number of stars. A well-identified peak around GPA = 80° shows an FWHM of about 55° above a uniform pedestal of 2.5% per bin containing about 45% of the stars. The gray curve connecting open triangles shows the cumulative distribution and is used to identify the median GPA of 75°, which is well offset from the 90° expected for a magnetic field perfectly aligned with the Milky Way disk.

This average orientation of starlight polarizations in the Galactic disk provides key information about the large-scale structure of the Galactic magnetic field. The Galactic magnetic field can be decomposed into two orthogonal components, the toroidal and poloidal magnetic fields (Moffatt 1978). For $|b| < 1°$, the projected toroidal field will be aligned with GPA = 90° and the projected poloidal field is generally aligned with GPA = 0° for the longitudes spanned by GPIPS. Since the total magnetic field is the vector sum of the poloidal and toroidal components, the average orientation of the starlight polarizations can inform estimates of the relative strengths of the toroidal and poloidal components, as

$$\frac{B_{\rm TOROIDAL}}{B_{\rm POLOIDAL}} \approx \tan(\langle {\rm GPA} \rangle), \qquad (1)$$

where $B_{\rm TOROIDAL}$ is the average toroidal magnetic field component and $B_{\rm POLOIDAL}$ is the average poloidal magnetic field component, both projected onto the plane-of-the-sky. For an average GPA of 75°, the ratio of strengths of the projected toroidal and poloidal fields is 3.7. This is in agreement with the general prediction that for a disk-symmetric Galactic magnetic field the toroidal magnetic field should be larger than the poloidal component (e.g., Ferrière & Schmitt 2000).

5.3. Medium-scale Magnetic Field Deviations

The GPA values of the DR1 UF = 0 stars were binned with Galactic longitude ℓ to explore medium-scale behavior of the magnetic field, as shown in Figure 25. To construct this figure, the unweighted GPA values for the UF = 0 stars were binned by longitude. Means, dispersions, and uncertainties were calculated and are shown in the figure as points, vertical dotted lines, and the gray zone, respectively. Changing to weighted means and uncertainties has little effect on the behaviors revealed in the figure. Longitude bins absent in the DR1 sample are seen as the absence of plotted means and dispersions near $\ell = 38°$ and 19°. Positive excursions of the mean polarization position angle by 30°–40° near $\ell = 45°$ and 30° may be associated with the FP decreases near those longitudes, already shown in Figure 7, while mean GPA excursions to smaller values near $\ell = 54°$, 34°, and 24° match well to FP increases. A detailed comparison awaits completion of GPIPS, as biases are certainly present in this limited data set.

The dependence of measured polarization percentages versus GPA for the UF = 0 subsample is displayed in contours of stellar density in Figure 26. The highest density of stars occurs for $P \sim 1.5\%$ at GPA = 80°–90°. The population of stars near this range of GPA tends to extend to the highest P values in UF = 0, indicating that they are probing to large distances in the Galactic disk. A second population appears to span virtually all GPA values with mean polarizations of under 2%. This feature likely arises from stars probing nearby magnetic field structures that must also exhibit significant GPA departures from the central values.

These first, crude characterizations of the polarization and directional properties of the UF = 0 subsample drawn from the UF = 1 sample in DR1 reveal interesting aspects of the Galactic magnetic field that are newly uncovered, and ones which will be uniformly sampled as the GPIPS observations are completed, reduced to high-quality data, and released for analysis.

5.4. Polarimetry below S/N 1

The stellar entries in the POLCATs are dominated in number by the stars with low polarimetric S/N: the UF = 2 and UF = 3 samples. These stars were retained in the POLCATs despite their high uncertainties because the Gaussian nature of the Stokes U and Q quantities permit averaging sets of stars to form mean values of P and P.A. with useful scientific content. In the two

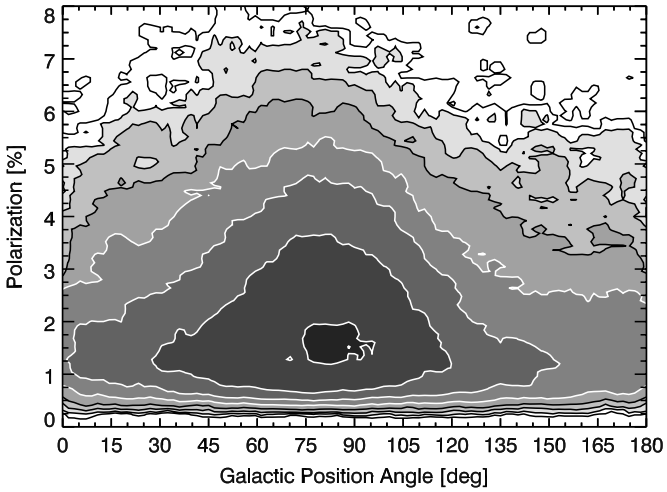

Figure 26. Distribution of polarization percentage P with Galactic position angle (GPA) for the UF = 0 subsample. Highest filled contour represents 90% of the peak stellar density in the plot and contour steps drop by half each. The excess of higher polarization stars for GPAs near 80° matches the peak in the GPA number histogram, showing that the most common GPA values are associated with higher polarizations, tracing the magnetic field deeply into the Galactic disk. The pedestal of GPA values in that histogram is seen here at all GPAs as polarizations up to about 2%, likely revealing relatively nearby magnetic field distributions are also being sampled. The lack of polarizations below about 0.5% is a selection effect characterizing the high-significance UF = 0 subsample.

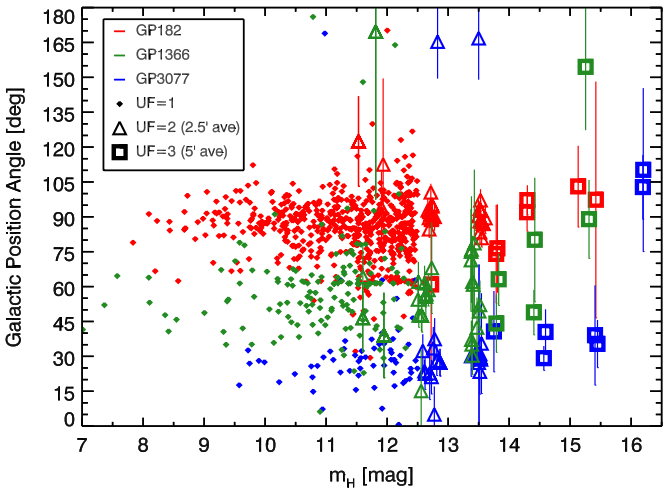

Figure 27. Galactic polarization position angles for fields GP182 (in red), GP1366 (in green), and GP3077 (in blue). Plotted as filled small diamonds are the UF = 1 high-quality individual stellar polarizations for each field. Open triangles with vertical $\pm 1\sigma$ error bars are the UF = 2 data, using weighted U, Q averaging over regions of size 2.5 × 2.5 arcmin^2 and 1 mag of faintness range. Open squares and error bars are the UF = 3 data, averaged over 5 arcmin sided boxes and 1 mag of faintness.

examples below, this averaging was done first by UF value (and then magnitude) and, second, by magnitude alone.

5.4.1. UF-based Averaging

An example to highlight the advantages of the choice to not cull low-S/N stars from the POLCATs was explored in some detail. In it, the magnetic field directions traced by the high-quality UF = 1 stars were compared to average field directions deduced from combining many UF = 2 and UF = 3 stars. Not only do the UF = 2–3 samples show many of the same properties as the UF = 1 sample, they allow probing to fainter apparent magnitudes and are thereby likely probing to farther distances. As such, they likely reveal changes of the magnetic field with distance along the line of sight.

Information contained in the UF = 2 and UF = 3 samples was revealed by computing the average polarization properties for groups of stars selected from extended sky regions and across magnitude ranges. This was done for data drawn from three of the five fields already shown, GP182 (Figure 8), GP1366 (Figure 10), and GP3077 (Figure 12). For each of these fields, the UF = 1, 2, and 3 samples of stars were separately selected from the POLCATs.

The GPAs for the UF = 1 stars are plotted versus H-band magnitude in Figure 27 as filled diamonds, with colors identifying which field supplied the stellar information. The inner Galaxy field GP182 (in red) shows stars with GPA values close to 90° with about 10° of scatter for the brighter magnitudes, rising to about 30° of scatter by $m_H \sim 12.5$ mag. The intermediate longitude field GP1366 (in green) shows a larger scatter, with a mean GPA closer to 60°. The high longitude field GP3077 (in blue) has smaller GPA scatter about a mean of about 25°.

The more numerous UF = 2 entries were binned in two ways and then weighted averages were computed. Across each of the three fields, the R.A. and decl. extents were divided into four zones, yielding 16 regions each of about 2.5 × 2.5 arcmin^2. Within each region, UF = 2 stars were further collected into magnitude-based bins, each spanning 1 mag. For each solid-angle/mag bin containing multiple UF = 2 stars, weighted averages and uncertainties were computed for the Stokes U and Q quantities. These were combined to form P and GPA and their uncertainties. In Figure 27, these mean GPA values and uncertainties are plotted as open triangles, at the location of the mean H-band magnitude for the stars in each bin. The high density of these overlapping triangles (in the colors corresponding to their GP field numbers) at the *same* GPA values favored by the UF = 1 stars for each field shows that the magnetic field traced by the UF = 1 stars is still being traced in the UF = 2 stars and to fainter magnitudes than the UF = 1 stars can reach.

The same binning by solid angle and magnitude was performed on the UF = 3 stars for each field. Here, the angular bins were quadrupled in solid angle, to roughly five arcmin on a side (similar to the resolution of *Planck*; Ade et al. 2011). Note that as with the UF = 2 binning, some UF = 3 bins of stars with solid angle and magnitude contain no entries, so the numbers of plotted symbols at each magnitude may not equal the maximum possible. The mean GPA, uncertainties, and mean H-band magnitude values are plotted as open squares and vertical error bars, also in the corresponding GP field colors. Here, two effects seem to be present. For the brighter UF = 3 mag, those around $m_H \sim 13$–14, the UF = 3 GPA values mostly follow the UF = 1 and UF = 2 GPA values. However, for GP1366 and GP3077, the two fields that show strong departures from the GPA = 90° value characterizing a pure toroidal magnetic field, the fainter UF = 3 stars, when binned, move *closer* to GPA = 90°. For example, the blue filled small diamonds for GP3077 show GPA values near 25° and the blue open triangles show the same mean GPA. The open blue squares at $m_H \sim 13.5$ reveal GPAs closer to 35°, which persist to $m_H \sim 15.5$. But the faintest UF = 3 stars in GP3077, those with $m_H \sim 16.5$, show GPA values much closer to 90°. The green open triangles and open squares for GP1366 show a similar trend, of agreeing with the UF = 1 GPA of 60° at the brighter magnitudes, but at the fainter magnitudes they move closer to GPA = 90°.

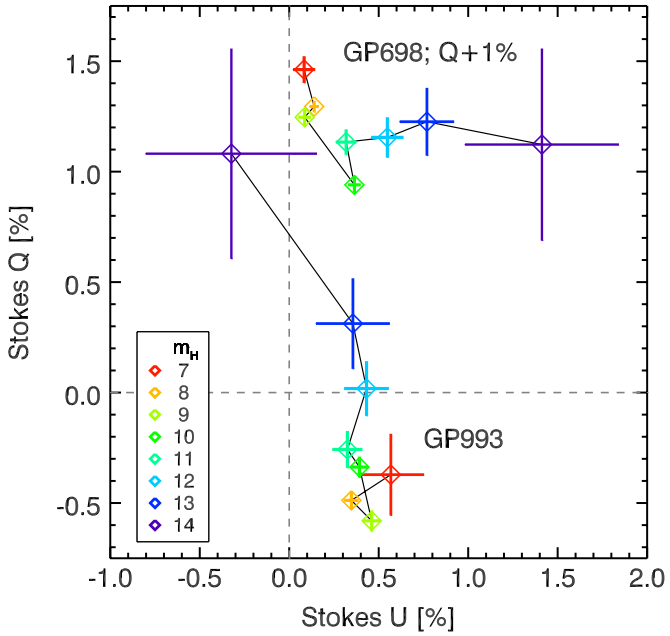

Figure 28. Stokes Q as a function of Stokes U for magnitude-binned weighted-averages for the GP698 and GP993 fields, colored by H-band magnitude of the bin. Error bars show $\pm 1\sigma$ uncertainties of the mean values. The GP698 values have been offset by +1% in Q for clarity. In these fields, the mean U and Q values are seen to change systematically with stellar magnitude, indicating changes in the magnetic field with either extinction or distance, or both. Legend in lower left identifies colors and bin magnitudes. Dashed lines through (0, 0) identify the location of zero polarization.

(A color version of this figure is available in the online journal.)

Interestingly, the GP182 (red symbols) field shows no such GPA rotation—its UF = 1, 2, and 3 stars stay close to the GPA = 90° value for H-band magnitudes from 8 through 15.5.

If the mean H-band magnitude can be interpreted as a proxy for stellar distance, by assuming all stars are of the same spectral type and luminosity class (K-giants, say), then one interpretation of the behaviors seen in Figure 27 is that the fields GP1366 and GP3077 show regions of coherent magnetic field that are misaligned with the dominant planar toroidal field over some size scales, but that eventually the magnetic field settles back to being toroidally dominated, or samples enough small-scale GPA $\neq$ 90 regions to polarimetrically average to GPA = 90. It will be important to measure the sizes and properties of these coherent magnetic features and to test how they relate to supernovae and the local interstellar medium.

5.4.2. Magnitude-based Averaging

Another way to probe changes in the magnetic field with distance is to follow the changes in Stokes U and Q as a function of stellar brightness, as shown in Figure 28. There, POLCAT values derived from two of the GPIPS fields, numbers 698 and 993, have been binned by H-band magnitude (independent of UF value) into unity-wide magnitude bins and the weighted U and Q, and their uncertainties, were calculated. Each of these average (U, Q) pairs is plotted, with $\pm 1\sigma$ error bars shown for both axes and solid black lines connecting consecutive points. The degree of polarization is the radial offset from the (0, 0) position (marked by the crossed, dashed gray lines) and the position angle is related to half the arctan of the (U/Q) ratio. Thus, the wander of the points as a function of stellar magnitude indicates systematic changes in the magnetic field. Stellar magnitude changes could result from extinction changes or from distance, and both could be present. Also, to enable detailed determination of how the magnetic field is changing, radiative transfer for Stokes parameters must be applied (Martin 1974; Pavel 2011), as distant stars probe the entire line of sight, including the magnetic fields being traced by more nearby stars. Despite these concerns, one (oversimplified) interpretation of Figure 28 is that the (U, Q) systematic wander reveals magnetic field changes with distance and may offer the opportunity to test magnetic field models with three-dimensional observational information.

6. CAVEATS AND WARNINGS

There are several concerns regarding the DR1 data and, by extension, the full GPIPS data set that bear consideration.

The single-waveband, single-epoch nature of the polarization measurements will yield incorrect polarization properties for objects with strong polarimetric time variability. A multi-epoch survey of a star-forming region by K. Covey (2011, private communication) using Mimir reveals substantial polarization variations for many of the YSOs. GPIPS observations overlapping Galactic plane star formation regions will be affected.

The data processing pipelines (Paper I), though based on building robust PSF models that can vary across the FOV, are not immune to problems introduced by close stellar doubles. We have modeled these conditions, with various input polarizations for the members of stellar doubles, with ranges of brightness ratios, separations, and position angles. The general conclusion is that for model stars with centers separated by at least one FWHM of the PSF, the software is able to recover the input polarization properties. The warning, though, is that there has been no checking or culling of the entries in the POLCATs to test for doubles exhibiting smaller separations.

The strong field-flattening applied in the data pipelines to enhance detection and PSF fitting of stars in each GPIPS field represents a strong spatial filter that removes most large-scale excess surface brightness. That is, clouds with bright rims, which occur due to reflection of diffuse Galactic light or nearby stars, will not show such extended structure in the combined GPIPS FITS images. Similarly, infrared dark clouds will not show surface brightnesses lower than their surroundings, though they will be apparent through their lower stellar surface densities of background stars.

Bright stars produce several problems. In addition to often showing saturated cores, so that photometry (using our current software) is not possible, they can often produce diffraction spikes due to the Perkins telescope secondary support spiders (these are at 45° from the equatorial directions). Very bright stars can also produce row and or column "bleeding," and occasional row "pull down" effects. These effects are normally limited to the one quadrant of the detector array containing the bright star(s). Detection of fainter stars in the PSF skirts and the spikes is difficult, due to S/N thresholds, so expect artificial deficits of fainter stars near bright ones. "Ghost" stars, due to internal reflections in the Mimir instrument, are well rejected through the design of the optics (Clemens et al. 2007). While ghost reflections will appear in some images, no unsaturated star generates detectable ghosts, and all saturated star ghosts are broader than the PSFs and so easily rejected in the pipeline processing steps.

Because of the spatial filtering and the additional problems introduced by strong stellar crowding, completeness of stellar detections and polarization measurements for high-density star clusters is unlikely. Calibration observations of globular clusters

(Paper II) has already shown the difficulty of measuring stellar polarizations in the cores of these clusters, given the typical seeing at the Perkins and the relatively large pixel size employed.

The increased polarimetric uncertainty for stars brighter than 8th mag (see Figure 16) is not currently understood, and will be examined for either resolution or explanation prior to future data releases.

The photometric utility of GPIPS is not comparable to that of multi-band surveys. At present, stars in each GPIPS field have their *H*-band photometry tied directly to the matching 2MASS stars in the field. On average this works well, and color effects are not excessive. Our *H*-band internal photometric uncertainties are far below those of 2MASS, which may be correct for star-to-star comparisons within the same GPIPS field but fails to capture all of the systematic uncertainties. Our comparisons, including the repeat observations of the same GPIPS fields, reveal the need to include a 45 mmag external uncertainty term.

At present, there are no plans for combining the stellar (or image) data for overlapping fields or portions of fields. We believe there is higher value in releasing data with a field-based organizational structure at this time, to permit others to examine multi-epoch polarization and photometric behavior. Once GPIPS is completed, more comprehensive and uniform data products may be developed and released.

7. SUMMARY

GPIPS, a near-infrared *H*-band linear polarization survey of some 76 deg^2 of the mid-plane region of the first Galactic quadrant, is nearly complete. Data processing and calibration have progressed to the point where release of science-quality data to the community of potential users is warranted. Here, public release of GPIPS data products encompassing 559 (17%; the "DR1" set) of the 3237 individual 10 × 10 arcmin GPIPS fields is announced. In addition to describing the forms and structures of the release data, initial example science explorations and highlights are offered.

The DR1 data products include, for each of the fields: (1) a summary plot, in Postscript form, showing an *H*-band image of the field and the most significant linear polarization detections as vectors and significant polarization upper limits as circled stars; (2) a combined (deep) photometric *H*-band FITS image, with an overlay file showing the polarizations and upper limits, color-coded by S/N; (3) a PHOTCAT file containing the stellar photometry of stars found in the FITS image, down to about 17th mag; and (4) a POLCAT file containing the stellar polarimetry, for all stars with sufficient brightness measurements in each of the four independent HWP polarization position angles.

These data were shown to reveal Galactic features as distant as the central bulge, as well as correlations of polarization properties with spiral arms. The mean plane-of-the-sky polarization (and thereby magnetic field) direction is mostly along the Milky Way disk, but does show a 15° offset for this DR1 sample, allowing assessment of the relative strengths of the toroidal and poloidal field components for the Galaxy.

Unique to the GPIPS approach, stellar polarizations are included in the POLCATs that, formally, are non-detections. However, the large numbers of such values, combined with the Gaussian nature of the Stokes *U* and *Q* quantities, permits forming spatial or magnitude binned averages to reveal magnetic field properties of the ISM. These are found to both agree with the field properties revealed by the significantly detected stellar polarizations and to probe to distances farther than possible for nearly all of the brighter stars.

Three samples of stellar polarizations were formed, using a UF value based on stellar brightnesses and polarization uncertainties. The UF = 1 stars, those capable of being used individually as background probes for foreground magnetic fields, have $m_H < 12.5$ and $\sigma_P < 2\%$. On average, there are about 300 of these stars in each 10 × 10 arcmin GPIPS field. The UF = 2 and 3 samples represent, respectively, successively fainter stars with higher polarimetric uncertainties. These samples require averaging to yield lower-resolution magnetic field maps, but represent a further 1,400 stars per GPIPS field for analysis.

Using the DR1 fields as a basis, the full GPIPS data set is expected to contain about 5.6 million stellar polarization measurements, of which about one million will be UF = 1 stars. This represents an enormous leap in availability of stellar polarization data and is expected to reveal the magnetic nature of the Milky Way disk in new and interesting ways.

In addition to the authors, these GPIPS observations were conducted in part by April Pinnick, Julie Moreau, Robert Marchwinski, Meredith Bartlett, and Christine Trombley. This publication makes use of data products from the Two Micron All Sky Survey, which is a joint project of the University of Massachusetts and the Infrared Processing and Analysis Center/California Institute of Technology, funded by NASA and NSF. This research was conducted in part using the Mimir instrument, jointly developed at Boston University and Lowell Observatory and supported by NASA, NSF, and the W. M. Keck Foundation. The GPIPS effort has been made possible by grants AST 06-07500 and AST 09-07790 from NSF/MPS to Boston University and by grants of significant observing time (BU key project status) from the Boston University—Lowell Observatory partnership.

Facility: Perkins

APPENDIX

GPIPS DATA PRODUCTS: TYPES AND STRUCTURES

The data products comprising this first data release of GPIPS data consist of images and plots for each of the 559 observed sky fields as well as tables of photometry and polarimetry for the stars in each field. DR1 data may be fetched from the GPIPS data portal (http://gpips0.bu.edu) and from mirror sites. In the following, each of these products is described as to form and structure. Associated metadata and data record entries are described and examples provided.

A.1. Overview Plots

One summary plot, showing a representation of the *H*-band combined photometric image with overlaid highly significant polarization vectors, is provided for each of the observed fields. Examples of these summary plots were shown in Figures 8 through 12. Axes are labeled with J2000 epoch R.A. and decl. values, and the GPIPS field number designations appear as title lines. The images are logarithmically stretched to show some of the fainter aspects of the images as well as the brightest stars, some of which appear saturated. The vectors drawn have polarization S/N at or above 2.5. Important polarization upper limits are deemed to be those with S/N under 2.5 and *P* values under 1%—these are shown as open circles. Note that these S/N selections are not equivalent to the UF designations described

Table 3
DS9 Region Files Color-thickness Coding

Type (1)	Range (2)	Color (3)	Thickness (4)
Detections	>10 S/N	Red	Thickest
	7–10 S/N	Yellow	Thick
	4–7 S/N	Cyan	Medium
	2–4 S/N	Green	Thin
	1.25–2 S/N	Magenta	Thin
Upper Limits	0.0%–0.1% P	Red	Thickest
	0.1%–0.3% P	Yellow	Thick
	0.3%–0.6% P	Cyan	Thin
	0.6%–1.0% P	Magenta	Thin

in the text, but are intended to reveal overall magnetic field directions and a sense for the degree to which the field appears coherent or non-coherent. These plots exist as Postscript files.

A.2. FITS Images and DS9 Overlays

FITS images of the photometric image combination of all of the 96 (to 117) images for each polarimetric observation of a sky field are provided, as are overlay "region" files for use with DS9 (Joye & Mandel 2003). The FITS images are presented as single-precision floating point values. The pixel data values are the linearity-corrected detector analog-to-digital converted counts scaled to the sum of the images shown.

Metadata in the FITS header include coordinate quantities supporting the FITS World Coordinate System (WCS; Calabretta & Greisen 2002) for a tangent projection, information regarding observations of the field (operator, date, time, air mass, filter wheel positions and encoding, environmental characteristics, etc.), history of data processing (dates, software version numbers, operator, correction file names), and values either found or selected for data processing and analysis (FWHM, saturation limit, PSF fitting radius, number of PSF stars, radii used for aperture photometry, the positional offsets and relative scale factors applied to constituent images, and related information).

The DS9 overlay region files contain all of the information shown as the vectors and open circles in the summary plots, with the addition of color-coding by polarization detection (or upper limit) S/N, as listed in Table 3. The S/N cutoff is also lowered to 1.25. Upper limits are represented as colored open circles, with the colors and circle thicknesses coded by polarimetric uncertainty σ_P. Detections are shown as vectors, whose lengths encode the polarization percentage P and whose angles encode the equatorial position angle of the linear polarization. Vector colors and thicknesses encode the polarization S/N. Each DS9 region file also contains a white reference vector in the lower left of the image with a label identifying the mapping of that vector length to percentage polarization.

A.3. PHOTCAT and POLCAT Files

The PHOTCAT files, one per field, report the photometric findings for each field, as derived from the deep combined images (the FITS images described above). The PHOTCATs are ASCII files that consist of a "header" containing metadata for the field, presented in a FITS-like "keyword – value" format, followed by record lines (one per star) containing multiple fields of values for each star. The PHOTCAT and POLCAT files for each field contain the same metadata. The metadata fields are listed in Table 4 with names, example values, and descriptions.

Table 5 lists the data fields in each star record that are in both the PHOTCATs and POLCATs, gives values for one star, and describes the variables, while Table 6 lists the POLCAT-only data fields that report the polarization information.

In Table 4, many of the field descriptions are sufficient, but a few require more explanation. The NGROUPS field will always be unity for GPIPS data, as repeat observations of fields are not combined. However, in other data sets developed with the PhotoPOLarimetry (PPOL; Paper I) software, combining of multiple observations is both possible and practiced. In those cases, NGROUPS will exceed unity and the fields following NGROUPS will be duplicated, one per observation (each encompassing some 96–117 images). Hence, the "01" suffices for those variables will be incremented for each additional constituent observation in the combination. Second, the average stellar profile FWHM is indicated twice. The first is the value as measured from the mean image stellar profile, while the second reports a corrected value that takes into account the relatively large pixels (0.58 arcsec) used. The remaining fields report the findings for the images and scaling aspects as determined in the data processing steps. These include the number of images originally observed as part of the group, the number of those images subsequently rejected by the analysis software, the mean sky, the sky noise measured by the image-to-image relative scaling step, the FP, its uncertainty, and the root-mean-square of the scaling factors found (all of these quantities are described in Paper I).

In Table 5, each star found by the PPOL software in each field is given an identifying number and a coordinate-based designation. The location of each star on the deep photometry FITS image is listed, followed by the effective location of that star on the detector array. The latter is important, as the hex-pattern sky-dither places each star at somewhat different detector locations and the instrumental polarization corrections are based on detector positions, not astrometrically registered and combined final image coordinates. The mean locations are the average of the hex dither locations and were used to index the $P_{\rm INST}$ correction for each star. Equatorial coordinates are those returned by the astrometric solutions for each GPIPS field, based on the 2MASS stars found in each field. The H-band magnitude is the internal instrumental magnitude for the star in the frame, measured using the PSF-cleaned aperture photometry of the best aperture (Paper I). These have been corrected by the mean difference between the 2MASS H-band magnitudes and the Mimir-measured H-band magnitudes for the typically 200–500 matching stars in the field. The "sHmag" quantity is the internal uncertainty, returned by the aperture photometry, and is appropriate for star-to-star comparisons within a field. The "sPhot" quantity is the root square sum of sHmag with 45 mmag, to provide an estimate of the external magnitude uncertainty, for comparison with H-band values from other catalogs. The group number identifies stars that were judged to need simultaneous PSF fitting in order to determine their brightnesses (see Paper I).

The next two groups of fields were drawn directly from 2MASS (Skrutskie et al. 2006) and GLIMPSE (Benjamin et al. 2003) data, fetched from the Vizier Service of the Centre de Donnes astronomiques de Strasbourg. As described in Paper I, stars observed for GPIPS were matched to 2MASS stars in each field, based on positions and magnitudes. GLIMPSE data were not matched independently to GPIPS stars, but were instead selected by matching 2MASS name designations. That is, the

Table 4
PHOTCAT and POLCAT Metadata

Name (1)	Example Value (2)	Description (3)
GPOBSRUN	201005	Observing run—YYYYMM
GP_GROUP	GP3195	GPIPS field designation
PPOL_VER	v7.1.0 20120501	Software version number, date
DTM_PPOL	Tue Feb 21 16:07:40 2012	Date, time of analysis
AXIS_ABR	1.1262	PSF average A/B axis ratio
NGROUPS	1	Number of groups (>1 = Meta-Group)
IMAG_A01	20100523.988_LDFC.fits	First image in group
IMAG_Z01	20100523.1089_LDFC.fits	Final image in group
JDMEAN01	2455339.7618321	Mean Julian date/time
FWHMAV01	1.980	Average FWHM (arcsec)
FWHMCR01	1.893	FWHM corrected for pixel sampling (arcsec)
NINGRP01	102	Number of images observed for this group
NUSE0_01	0	Number of images rejected from combinations
AV_SKY01	80.589	Mean sky (ADUs per pixel per second)
SKNOIS01	0.555	Mean sky noise after scaling (%)
FLDPOL01	1.308	Mean field polarization found by scaling step (%)
S_FLPL01	0.102	Uncertainty of field polarization (%)
RMSSCL01	0.007	rms of atmospheric scale factors (mag.)

Table 5
PHOTCAT and POLCAT Common Data Record Fields

Name (1)	Example Value (2)	Description (3)
ID	0	Star number in field (from 0)
Desig	GPIPS_J193221.38+195509.6	GPIPS-based star designation
X_img	1048.32	Star center *X*-location in FITS image (pixels)
Y_img	212.08	Same, for *Y* (pixels)
X_det	1021	Mean *X*-location on detector (pixels) (for $P_{\rm INST}$ correction)
Y_det	185	Same, for *Y* (pixels)
RA_deg	293.089094	J2000 R.A. of Star (deg)
Dec_deg	19.919325	Same, for Decl. (deg)
H_mag	13.6278	GPIPS *H*-band star magnitude
sHmag	0.0778	Internal uncertainty in *H*-band magnitude
sPhot	0.0899	External uncertainty in *H*-band magnitude
Sky_cts	20706.7	Local sky value around this star (counts)
Group	3390	DAOPHOT Group containing this star
	2MASS Fields	
ID_2MASS	0	Star number in field (from 0)
Desig_2MASS	J19322137+1955098	Designation
RA_2MASS	293.089074	J2000 R.A. (deg)
Dec_2MASS	19.919416	J2000 Decl. (deg)
J_2MASS, sJ2MASS	14.925, 0.059	*J*-band magnitude and uncertainty
H_2MASS, sH2MASS	13.739, 0.046	Same, for *H* band
K_2MASS, sK2MASS	13.163, 0.041	Same, for *Ks* band
	GLIMPSE Fields	
B3.6mag, E_B3.6mag	12.796, 0.061	Band 1 (3.6 μm) magnitude and uncertainty
B4.5mag, E_B4.5mag	12.735, 0.155	Same, for Band 2 (4.5 μm)
B5.8mag, E_B5.8mag	12.718, 0.280	Same, for Band 3 (5.8 μm)
B8.0mag, E_B8.0mag	12.405, 0.248	Same, for Band 4 (8.0 μm)

GLIMPSE matching to 2MASS was done by the GLIMPSE team, leading to 2MASS associations. GPIPS utilizes that matching in listing the GLIMPSE brightnesses. Where 2MASS or GLIMPSE data are absent, or no match occurred, in-band magnitudes and uncertainties are set to values of 99.99. If no 2MASS star was matched to a GPIPS star, the 2MASS designation was set to "_2_none_."

POLCAT data files contain all the same fields as PHOTCAT data files, but contain fewer star entries in addition to adding new data fields. POLCATs only list records for stars with data from all four IPPAs. The sixteen HWP observations at each sky dither could result in as much as a fourfold redundancy at each IPPA. However, only a very small fraction of the PHOTCAT stars meet the IPPA criterion, so only they are propagated into the POLCATs. Table 6 therefore contains two identifying numbers: one consecutive number for each star listed in a POLCAT, and an ID number that points back to the star's entry in the PHOTCAT file for the field. The remaining additional data fields in the

Table 6
POLCAT-specific Data Record Fields

Name (1)	Example Value (2)	Description (3)
Num	8	POLCAT ID number for this star (from 0)
ID	10	PHOTCAT ID number for this star
P	1.506	Linear polarization (%)
sP	0.773	Uncertainty in P (%)
P.A.	12.201	Equatorial position angle (E from N; deg)
GPA	73.348	Galactic position angle ($+\ell$ from $+b$; deg)
sPA	14.703	Uncertainty in either position angle (deg)
Q, sQ	1.542, 0.780	Stokes Q and uncertainty (%)
U, sU	0.699, 0.736	Stokes U and uncertainty (%)
nHWP	14	Number of HWP values for this star (max 16)
UF	1	Usage Flag (1, 2, or 3)

POLCAT-specific table report aspects of the measured linear polarization properties, beginning with the polarization degree P and its uncertainty σ_P, both as percentages. The P values are Ricean-corrected (see Paper I) for the effects of uncertainties on these positive-definite quantities. Two position angles are given, the first relative to equatorial coordinates (P.A.) and the second relative to Galactic coordinates (GPA). The uncertainty that follows pertains to both PA values. Next, the Stokes Q and U and their uncertainties are given (as percentages), followed by the number of HWP observations used for each star. Finally, the UF described in the text is given as an integer value between unity and three.

A.4. GPIPS-provided Software

To ease access to PHOTCAT and POLCAT data files, IDL functions were written to open, read, and parse these data files and to return IDL structures suitable for access and analysis. These functions are *read_photcat.pro* and *read_polcat.pro* and may be fetched from the GPIPS Web site (http://gpips0.bu.edu). Invoking either returns a two-part IDL structure. The first part contains all the header metadata, with tag names mapping to those listed in Table 4. The second part of the structure contains an array of structures, one per star, with tag names in each structure matching those listed in Tables 5 and 6.

REFERENCES

Benjamin, R. A., Churchwell, E., Babler, B. L., et al. 2003, PASP, 115, 953
Benjamin, R. A., Churchwell, E., Babler, B. L., et al. 2005, ApJ, 630, 149
Bessell, M. S., & Brett, J. M. 1988, PASP, 100, 1134
Calabretta, M. R., & Greisen, E. W. 2002, A&A, 395, 1077
Casali, M. M. 1995, MNRAS, 277, 1385
Clemens, D. P., Pinnick, A. P., & Pavel, M. D. 2012a, ApJS, 200, 20 (Paper II)
Clemens, D. P., Pinnick, A. P., Pavel, M. D., & Taylor, B. W. 2012b, ApJS, 200, 19 (Paper I)
Clemens, D. P., Sarcia, D., Grabau, A., et al. 2007, PASP, 119, 1385
Ferrière, K., & Schmitt, D. 2000, A&A, 358, 125
Jones, T. J. 1989, ApJ, 346, 728
Jones, T. J., Klebe, D., & Dickey, J. M. 1992, ApJ, 389, 602
Joye, W. A., & Mandel, E. 2003, in ASP Conf. Ser. 295, Astronomical Data Analysis Software and Systems XII, ed. H. E. Payne, R. I. Jedrzejewski, & R. N. Hook (San Francisco, CA: ASP), 489
Lada, C. J., Lada, E. A., Clemens, D. P., & Bally, J. 1994, ApJ, 429, 694
Lada, C. J., Muench, A. A., Haisch, K. E., Jr., et al. 2000, AJ, 120, 3162
Lombardi, M., & Alves, J. 2001, A&A, 377, 1023
Martin, P. G. 1974, ApJ, 187, 461
Meyer, M. R., Calvet, N., & Hillenbrand, L. A. 1997, AJ, 114, 288
Moffatt, H. K. 1978, Magnetic Field Generation in Electrically Conducting Fluids (Cambridge: Cambridge Univ. Press)
Pavel, M. D. 2011, ApJ, 740, 21
Planck Collaboration:, Ade, P. A. R., Aghanim, N., Arnaud, M., et al. 2011, A&A, 536, 1
Rieke, G. H., & Lebofsky, M. J. 1985, ApJ, 288, 618
Serkowski, K., Mathewson, D. S., & Ford, V. L. 1975, ApJ, 196, 261
Simpson, J. P., Burton, M. G., Colgan, S. W. J., et al. 2009, ApJ, 700, 1488
Skrutskie, M. F., Cutri, R. M., Stiening, R., et al. 2006, AJ, 131, 1163
Sogawa, H., Tamura, M., Gatley, I., & Merrill, K. M. 1997, AJ, 113, 1057
Whittet, D. C. B. 2003, Dust in the Galactic Environment (2nd ed.; Bristol: IOP)
Wilking, B. A., Lebofsky, M. J., Kemp, J. C., et al. 1980, ApJ, 235, 905